



Optimal control and performance evaluation of an inerter-based point absorber wave energy converter

Tao Sun^{a,b}, Zili Zhang^{c,d,*}

^a College of Engineering, Ocean University of China, Qingdao 266100, China

^b School of Engineering and Material Science, Queen Mary University of London, London, E1 4NS, UK

^c Department of Civil and Architectural Engineering, Aarhus University, 8000 Aarhus, Denmark

^d State Key Laboratory of Disaster Reduction in Civil Engineering and College of Civil Engineering, Tongji University, Shanghai 200092, China

ARTICLE INFO

Keywords:

Wave energy converter
Point absorber
Optimal control
Inerter
Analytical solutions

ABSTRACT

This paper deals with optimal tuning, control and performance evaluation of an inerter-based point absorber (IPA) wave energy converter (WEC), which is a first step towards establishing an integrated offshore wind-wave energy system. An inerter-spring system is introduced into a conventional WEC, which can improve the system performance when properly tuned and controlled. Analytical expressions of the optimal IPA parameters have been derived under regular waves. Closed-form solution of the capture width ratio of the IPA under optimal control is obtained and verified by the theoretically optimal solution of a point absorber. Next, hybrid and passive control strategies for the IPA are also investigated, demonstrating superior energy absorption performance than the conventional point absorber under the same control strategy, due to the existence of an extra resonance and amplified motion of the inerter. Furthermore, the performance of passive IPA is evaluated under irregular waves, where parametric optimization has been performed with constraints on system modal frequencies. Single-mode and double-mode resonances have been observed for wave peak frequencies away from and close to the float natural frequency, respectively. This facilitates the frequency adaption of the IPA and the resulting superior performance in terms of more energy absorption and broader operational bandwidth.

1. Introduction

As two main types of the abundant offshore renewable energies, offshore wind and wave energies are considered to be promising alternatives to the conventional fossil energy resource, and they play an increasingly important role on the energy demand all over the world in the coming years. A possible cost-competitive strategy is to integrate offshore wind and wave energies into one system (Pérez-Collazo et al., 2015; Haji et al., 2018). The combined exploitation of wave and offshore wind energies on one hand can share the infrastructures, as well as operation and maintenance activities. On the other hand, the combined wave and offshore wind energy system can increase the availability of operational hours, improve the forecast accuracy of energy output and smooth power output. The combined system can finally enhance the energy yield and potentially reduce the overall levelized costs of energy (LCOE). It is known that wave energy is still at an early stage of development whereas offshore wind is a proven technology. Based on this, one possible way to achieve the combination of offshore wind and wave energies is integrating a wave energy converter (WEC) into an offshore wind turbine structure.

Utilizing the synergy between WECs and offshore wind turbines as hybrid converters, both wave energy and wind energy can be extracted by the system.

Modeling and testing of some integrated wind and wave systems have been carried out to investigate their synergy effect on the cost, power production and dynamic responses. Muliawan et al. (2013) proposed an integrated Spar-type floating wind turbine (FWT) and Wavebob-type WEC, and numerically investigated the effect of the heaving buoy on the FWT motions and power production under operational conditions. For wave and steady wind conditions, the addition of a heaving buoy could increase the stability of the Spar and thereby the wind power. It demonstrated the cost competitiveness and the total energy output enhancement of the integrated system. Afterwards, Gao et al. (2016) performed global dynamic response analysis of the aforementioned integrated system to investigate the coupling effect between the FWT and WEC motions. The numerical model could predict reasonably well most of the response quantities measured from a scaled model experiment. The similar numerical and experimental conclusions are applicable to an integrated system of a tension leg platform

* Corresponding author at: Department of Civil and Architectural Engineering, Aarhus University, 8000 Aarhus, Denmark.

E-mail addresses: t.sun@qmul.ac.uk (T. Sun), zili_zhang@cae.au.dk (Z. Zhang).

(TLP) type FWT and a heave-type WEC (Ren et al., 2020). Haji et al. (2018) used a symbiotic approach to design an integrated system by attaching an oscillating water column-type WEC array to a FWT. The results shown that the integrated system could not only reduce the WEC LCOE by sharing components but also increase the FWT tower fatigue lifetime by reducing the platform motion. Zhao et al. (2021) used a fully nonlinear model to comprehensively analyze the coupling effect between an FWT and a heaving buoy WEC. The fact that the WEC could significantly reduce the wind turbine pitch motion and effectively increase power production were demonstrated again. Furthermore, the relative heave motion between WEC and spar could buffer the maximum contact pressure. Also, the results shown how to design the power take off (PTO) system based on the quantification relationship between contact pressure and WEC peak power. Ren et al. (2018) proposed a new combined monopile wind turbine and a heave-type WEC system and performed the hydrodynamic response analysis under operational conditions numerically and experimentally. It demonstrated the feasibility of the combined system. Zhou et al. (2020) analyzed the hydrodynamic characteristic for an oscillating water column (OWC) type WEC integrated to a monopile type wind turbine, demonstrating the positive effect of the OWC to significantly reduce the horizontal force and overturning moment on the monopile numerically and experimentally. Cong et al. (2021) proposed a variation of the aforementioned integrated system of OWC WEC with four fan-shaped sub-chambers and monopile type wind turbine. Numerical results demonstrated a significant improvement of energy extraction efficiency for the proposed integrated system. Furthermore, the air compressibility in the sea chamber could make a negative effect on the wave power absorption. Si et al. (2021) investigated the influence of PTO control on the dynamic response and power output of a combined semi-submersible FWT and point-absorber WECs. Results shown that different PTO control strategies had considerable influences on the platform dynamics and power generation. Furthermore, the optimal control design for point-absorber WEC attached to fixed structures was shown to be no longer optimal for the combined platform. Wan et al. (2020) numerically investigated the dynamic responses of three integrated wind-wave converter concepts for deep, intermediate and shallow water depth conditions, respectively. The comprehensive study shown that dynamic responses of the three conceptual systems were significantly different, which could provide insights into further structural design and cost estimations.

The offshore wind is a proven technology, especially for fixed-foundation wind turbines that are considered as a mature technology with competitive LCOE comparing with fossil fuels. Therefore, to advance the development of integrated wind-wave systems, better design and understanding of the WEC device, as well as the way of installing the WEC to the wind turbine, should be paid more attention for further investigation. In recent years, the exploitation of wave energy attracts increasing attention across the world. To efficiently capture wave energy, various types of wave energy converters (WECs) have been developed, which can be roughly categorized as oscillating body, oscillating water column and overtopping device (Antonio, 2010). As a kind of floating oscillating body, a point absorber is the most investigated WEC due to its small size, low cost and simple construction (Beatty et al., 2019a). A point absorber is designed to resonate with the incoming wave in order to significantly capture wave energy but the resonance frequency of a point absorber does not usually coincide with the spectrum of the incoming waves, and real waves are spread over a wide range of frequencies so the effective frequency band to absorb the wave energy is mostly narrow. Therefore, it is often necessary to apply control strategies to force the WEC system into resonance. Optimal control strategies such as reactive control (Budal and Falnes, 1980; Falnes and Kurniawan, 2020), phase and amplitude control (Budal and Falnes, 1977), are initially proposed but they are frequency dependent. That means that optimal control policy will vary for each frequency, thus making its application difficult in irregular

waves. To circumvent this problem, stochastic optimal control based on variational principle (Nielsen et al., 2013) was proposed in time domain. Further, they are noncausal control strategies dependent of future information of WEC velocity or external wave excitation force. According to the phase and amplitude control, discrete sub-optimal latching control was proposed by Budal and Falnes (1978) to control the WEC system to increase the energy absorption through latching the WEC motion when its velocity is zero and releasing it when phases of WEC velocity and wave excitation force are identical. Compared with the optimal control, there is no reactive power in latching control, which can ease the requirement of high conversion efficiency. However, it is very challenging to determine when to latch and unlatch the WEC motion. Furthermore, the future wave information needs to be known in advance when applying latching control, which can be achieved by prediction algorithms but it is significantly more computationally complex and the prediction inaccuracy may cause the instability of this control, especially for broadband waves (Babarit and Clément, 2006).

Furthermore, in order to deal with difficulties in noncausal control, sub-optimal causal control laws have been proposed. For reactive control and phase and amplitude control, a causal transfer function is generally introduced to approximate the ideal non-realizable transfer function in effective frequency band (Clément and Maisondieu, 1993; Bacelli et al., 2019). For noncausal stochastic optimal control, causal stochastic optimal control is achieved using knowledge of the stationary spectral characteristics of the random sea state (Nielsen et al., 2013). For latching control, non-predictive latching control is proposed to control the point absorber (Sheng et al., 2015a,b) where latching duration is calculated as half a difference between the wave period and the WEC natural period, rather than using future wave information. However, they result in a narrow effective frequency band for WEC system to absorb the wave energy, especially for broadband waves.

Besides control strategies, a submerged float is attached to the semi-submerged float to shift the natural frequency of the system close to the wave excitation frequencies, which can increase the absorbed energy and broaden the effective frequency band (Wu et al., 2014; Beatty et al., 2015, 2019b). Piscopo et al. (2016) added a fully submerged body to the heaving buoy to properly shift the device's heave natural frequency to gain resonance with the most energetic waves and investigated the effect of the fully submerged added mass on captured energy. Liang and Zuo (2017) investigated the influence of the submerged body on the energy absorption of a two-body system and demonstrated its effective of power absorption in comparison to the single body system. Al Shami et al. (2019b) performed the parameter analysis of two-body WEC including a submerged body and revealed the shape of the submerged body had a significant effect on absorbed energy. Al Shami et al. (2019a) studied the improvement of the hydrodynamic performance of a point absorber by increasing the freedom degrees of the submerged bodies. Piscopo and Scamardella (2021) conducted the parametric design of a resonant point absorber equipped with a fully submerged toroidal shape to investigate the effectiveness of the new WEC device in terms of power production and cost of energy. Normally, the natural frequency of the semi-submerged body is much higher than frequencies of incoming waves. Although the inclusion of added submerged body can decrease the natural resonant frequency of the wave energy conversion and to increase the absorbed energy, this requires a submerged body with a huge mass, which increases the cost and the maintenance difficulties. Further, the effective frequency band for this two-body WEC is still narrow.

In the present paper, a compact and practically feasible design of an enhanced WEC is proposed, which has the potential of ease of installation to the wind turbine as well as the superior power absorption performance comparing with the conventional device. The inerter, which recently has been intensively studied for vibration control of civil engineering structures (Gonzalez-Buelga et al., 2017; De Domenico and Ricciardi, 2018), is introduced to the WEC for performance improvement. The inerter is a two-terminal mechanical device that can

generate an inertial force proportional to the relative acceleration between its two terminals, and the inertance with a unit of kilogram represents the proportionality constant (Smith, 2002). The device is able to transform the linear motion into high-speed rotational motion, resulting in a significantly amplified inertia force comparing with that generated by its physical mass (Papageorgiou and Smith, 2005). This is crucial for designing a lightweight high-performance device. Furthermore, more effective configurations can be realized by combining the inerter with spring and dashpot (linear viscous damper) (Ma et al., 2020; Zhang and Høeg, 2021), resulting in a mechanical system with superior vibration mitigation performance. The principle is that the inerter-spring-dashpot system constitutes a single-degree-of-freedom (DoF) system, and by properly tuning the system parameters (spring stiffness, inertance and damping coefficient), the motion of the vibration absorber can be in resonance with the structural vibration, so that more vibrational energy in the structure can be absorbed and dissipated by the mechanical system (Zhang and Larsen, 2021). This principle can be employed in WEC system for enhanced wave energy absorption, by incorporating a combined inerter-spring-dashpot system into the conventional WEC. Here, the inerter-based system for WEC is chosen where the inerter is coupled to the PTO system, which is then rigidly connected to the wind turbine structure. The PTO system and the float is connected by tuning springs. The resulting equivalent mechanical system constitutes an inerter in parallel with the PTO dashpot while in series with the connecting spring. A similar idea has been numerically investigated (Haraguchi and Asai, 2020; Sugiura et al., 2020) where the WEC is connected to seabed. As a result of the design, the PTO system is no longer directly coupled to the float motion, but instead directly coupled to the inerter motion. This facilitates increased wave energy absorption by making use of the amplified motion of inerter thus the PTO dashpot. By the introduction of inerter-based system, the enhanced WEC system becomes a 2-DoF system. As a relative motion device, the inerter has an effect on all the resonances in the proposed WEC system, which increases the potential to broaden the effective frequency band. However, this is only achievable by appropriately tuning (optimization) of the inertance, the spring stiffness and damping coefficient of the inerter-based system. While numerical optimization was performed for a similar device under limited load cases (Haraguchi and Asai, 2020), a comprehensive investigation on the optimal tuning of system parameters of an inerter-enhanced WEC is necessary for better understanding the mechanism and for robust design of the system under different environmental conditions.

The present paper aims to address the knowledge gap through establishing analytical expressions for optimal tuning of the inerter-enhanced WEC in regular waves and presenting a new optimization criteria for irregular waves. The mechanism of the proposed WEC is revealed from structural dynamics point of view, and different control strategies are investigated. The superior conversion efficiency of the proposed WEC comparing with the conventional WEC in terms of energy absorption and effective frequency band is demonstrated for different control strategies. The organization of this paper is as follows. Section 2 presents the working principle of the proposed inerter-based point absorber (IPA) WEC. Section 3 gives the hydrodynamic models for conventional point absorber (CPA) WEC and the IPA WEC. Section 4 derives the theoretical optimal power output in terms of capture width ratio (CWR) for both systems in regular waves, as well as the analytical expressions for optimal tuning of the IPA parameters. In Section 5, the active control, hybrid control and passive control for the proposed IPA WEC in regular waves have been investigated through numerical simulation in comparison to the CPA WEC, in terms of CWR and response amplitudes. Furthermore, the passive IPA is applied to irregular waves in Section 6. Following the proposed optimization criteria, the inertance, spring stiffness and damping coefficient of the proposed IPA WEC are determined leading to increased energy absorption and broadened effective frequency band in comparison to the CPA WEC.

2. Basic principle of the proposed inerter-based point absorber (IPA) WEC

The integrated wind and wave energy converters can share the infrastructures such as support structures, power substations, mooring systems and cables, and thus can effectively reduce the cost. Fig. 1 gives a schematic representation of one possible design of the integrated wind and wave energy converter system. This concept is inspired by the so-called spar torus combination (STC) (Muliawan et al., 2013), which combines a spar floating wind turbine and a torus-shaped, heaving point absorber WEC. In the present study, the torus-shaped point absorber is installed to the monopile of a fixed-foundation wind turbine system. As shown in Fig. 1(a), the point absorber can move along the monopile to absorb wave energy through a PTO system. Rollers and a mechanical system are employed to allow only the relative heave motions, as conceptually shown in Fig. 1(c). In the conventional design, the point absorber is rigidly connected to the PTO system, and thus the PTO is directly coupled with the float's oscillation. The conventional PTO system consists of a generator, whose rotation is driven by a pulley that is directly coupled to the heave motion of the float. When the PTO is represented by a linear spring-damper system, the conventional design can be simplified to an equivalent mechanical model shown in Fig. 2(a), where the mass moment of inertia of the pulley is neglected. Here m is the float mass, k_c and c_c are the damping coefficient and stiffness coefficient of the PTO system, respectively.

In the present study, the conventional design is modified. As shown in Fig. 1(a), tuning springs are installed between the float and the generator, so that the rotational motion of the generator is no longer directly coupled to the heave oscillation of the float. Besides, rotational inertial mass (with relatively small physical mass) is attached to the pulley of generator and rotates together with the generator, as shown in Fig. 1(b). Due to the rotational inertia, the small physical mass can produce an amplified equivalent mass effect when the translational motion is transformed into rotational motion. The amplification can be up to the order of a thousandfold, corresponding to the so-called mass amplification effect of the inerter (Wang et al., 2009, 2011). In practice, a flywheel with uneven mass distribution (more mass is distributed close to outer edge) can be employed as the rotational inertia (inerter). The equivalent mechanical model of the IPA WEC is illustrated in Fig. 2(b), again with the PTO being represented by a linear spring-damper system. Here k_2 is the effective spring stiffness from all tuning springs, and m_2 is the equivalent mass (inertance) of the inerter, as will be elaborated in Section 4. As seen, the inerter is combined in parallel with the spring-damper system of the PTO, which are connected to the float through the tuning spring in series.

In the following two sections, modeling and parametric optimization of the CPA WEC shown in Fig. 2(a) and the IPA WEC shown in Fig. 2(b) will be elaborated, respectively.

3. Conventional point absorber (CPA) WEC: modeling and optimization

Generally, a WEC is excited by the hydrodynamic force $f_h(t)$ and the control force $f_c(t)$ supplied by the PTO system used to extract the wave energy. Therefore, the equation of motion for the CPA WEC illustrated in Fig. 2(a) is:

$$m\ddot{u}(t) = f_h(t) - f_c(t) \quad (1)$$

where m is the float mass, $\ddot{u}(t)$ and $u(t)$ is the heave acceleration and displacement of the float, respectively. The control force $f_c(t)$ by the electromagnetic generator can be represented by a linear spring-damper system, expressed as:

$$f_c(t) = k_c u(t) + c_c \dot{u}(t) \quad (2)$$

with c_c and k_c being the damping coefficient and stiffness coefficient of the PTO system, respectively.

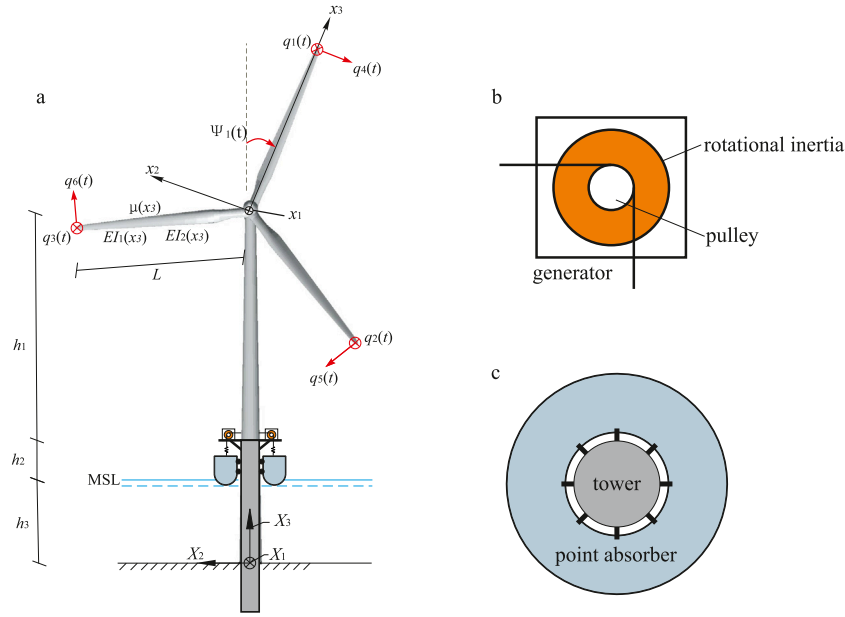


Fig. 1. Schematic representation. (a) Integrated wind and wave energy converter system. (b) Generator for the wave energy point absorber. (c) Top view of the combined system.

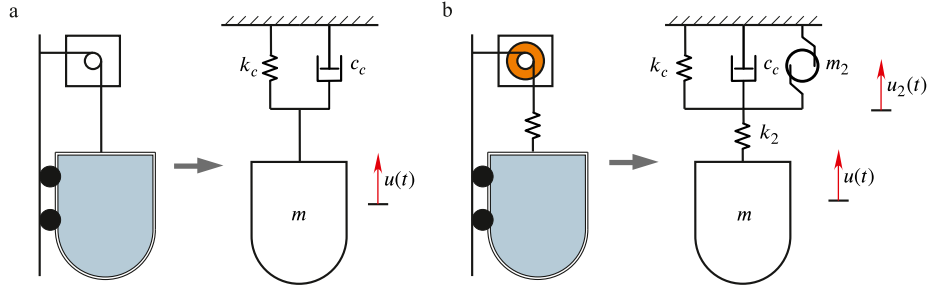


Fig. 2. Equivalent mechanical models. (a) The conventional point absorber (CPA). (b) The proposed inerter-based point absorber (IPA).

Based on the superposition principle of linear wave theory, the hydrodynamic force $f_h(t)$ can be expressed as:

$$f_h(t) = f_b(t) + f_r(t) + f_e(t) \quad (3)$$

where $f_b(t)$ is the restoring force from buoyancy. For small vertical vibration around the static equilibrium state (Newman, 2018), $f_b(t)$ can be expressed:

$$f_b(t) = -k_w u(t) \quad , \quad k_w = \frac{1}{4} \pi D^2 \rho g \quad (4)$$

where D is the diameter of the float, ρ is the mass density of water and g is the gravity acceleration. k_w is taken as the stiffness contribution from hydrostatic buoyancy.

$f_r(t)$ is the radiation force generated by the float motion in the absence of wave motion, which can dissipate the mechanical energy of the WEC by generating a wave train propagating away from the WEC, and it can be expressed as:

$$f_r(t) = -m_h \ddot{u}(t) - \int_{-\infty}^t h_{r\dot{u}}(t - \tau) \dot{u}(\tau) d\tau \quad (5)$$

where m_h is the hydrodynamic added mass at infinite high frequency, and $h_{r\dot{u}}(t)$ is the impulse response function for the radiation force driven by the float velocity $\dot{u}(t)$. The related frequency response function can be obtained as:

$$H_{r\dot{u}}(\omega) = \int_0^\infty e^{-i\omega t} h_{r\dot{u}}(t) dt \quad (6)$$

and the expressions related to the imaginary and real parts of $H_{r\dot{u}}(\omega)$ can be given as (Nielsen et al., 2013):

$$\left. \begin{aligned} M_h(\omega) &= m_h + \frac{1}{\omega} \text{Im}(H_{r\dot{u}}(\omega)) = m_h - \frac{1}{\omega} \int_0^\infty \sin(\omega t) h_{r\dot{u}}(t) dt \\ C_h(\omega) &= \text{Re}(H_{r\dot{u}}(\omega)) = \int_0^\infty \cos(\omega t) h_{r\dot{u}}(t) dt \end{aligned} \right\} \quad (7)$$

where $M_h(\omega)$ and $C_h(\omega)$ are the added mass and radiation damping coefficients for the monochromatic wave excitation, respectively.

$f_e(t)$ is the wave excitation force, which excites the WEC to move while transferring the wave energy to the mechanical energy of the absorber. The wave excitation force $f_e(t)$ can be obtained as:

$$f_e(t) = \sum_{i=1}^{\infty} 2\sqrt{S_{\eta\eta}(\omega_i)\Delta\omega} |H_{e\eta}(\omega_i)| \cos(\omega_i t - \phi_i + \theta_i) \quad (8)$$

where $S_{\eta\eta}(\omega)$ is the double-sided power density function for wave spectrum and $H_{e\eta}(\omega)$ is the frequency response function for the excitation force. $\phi_i = \arctan\left(\frac{\text{Re}(H_{e\eta}(\omega_i))}{\text{Im}(H_{e\eta}(\omega_i))}\right)$ represents the phase of excitation force response and θ_i is the random phase for wave generation. Note that the hydrodynamic parameters $M_h(\omega)$, $H_{r\dot{u}}(\omega)$, $H_{e\eta}(\omega)$ can be computed numerically using boundary element method-based programs (Lee and Newman, 2006; Babarit and Delhommeau, 2015).

Substituting Eqs. (2)–(5) into Eq. (1) provides the following equation of motion for the CPA WEC:

$$(m + m_h) \ddot{u}(t) + (k_c + k_w) u(t) + c_c \dot{u}(t) + \int_0^t h_{r\dot{u}}(t - \tau) \dot{u}(\tau) d\tau = f_e(t) \quad (9)$$

It is seen that the equation of motion for the CPA WEC represents a one degree-of-freedom (DOF) system with the integro-differential form. Under monochromatic wave excitation with the angular frequency ω , Eq. (9) becomes:

$$(m + M_h(\omega))\ddot{u}(t) + (k_c + k_w)u(t) + (c_c + C_h(\omega))\dot{u}(t) = F_e(\omega)\cos\omega t \quad (10)$$

where $F_e(\omega)$ specifies the amplitude of monochromatic excitation force, given as $F_e(\omega) = \frac{1}{2}H|H_{e\eta}(\omega)|$ with H being the wave height for regular wave.

Eq. (10) provides the following complex harmonic response $U(i\omega)$ of the float in the frequency domain, given as:

$$U(i\omega) = \frac{F_e(\omega)}{k_c + k_w - M(\omega)\omega^2 + i\omega(C_h(\omega) + c_c)} \quad (11)$$

where

$$M(\omega) = m + M_h(\omega) \quad (12)$$

Then, the frequency-domain transfer function $H_U(i\omega)$ between $U(i\omega)$ and wave height H is obtained as:

$$H_U(i\omega) = \frac{U(i\omega)}{H} = \frac{1}{2} \frac{|H_{e\eta}(\omega)|}{k_c + k_w - M(\omega)\omega^2 + i\omega(C_h(\omega) + c_c)} \quad (13)$$

whose amplitude (modulus) $|H_U(i\omega)|$ can be regarded as the normalized response amplitude of the float.

The time-average absorbed power through the PTO system becomes:

$$P = \frac{1}{2}c_c|U|^2\omega^2 \quad (14)$$

Substituting Eq. (11) into Eq. (14) provides:

$$P = \frac{1}{2}|F_e(\omega)|^2 \frac{c_c\omega^2}{(k_c + k_w - M(\omega)\omega^2)^2 + \omega^2(C_h(\omega) + c_c)^2} \quad (15)$$

To reflect the conversion efficiency of the WEC, capture width ratio (CWR) is introduced, which is defined as $P/P_{reg}/L_e$ where L_e is the wave length associated with the energy period T_e . P_{reg} represents the incident wave power per meter width of wave crest, which for regular wave can be expressed as (McCormick, 2013):

$$P_{reg} = \frac{\rho g H^2 c_g}{8} \quad (16)$$

where c_g is the group velocity of the incident wave given as:

$$c_g = \frac{c}{2} \left| 1 + \frac{2kd}{\sinh(2kd)} \right| \quad (17)$$

with d being the water depth, c being the phase velocity and k being the wave number.

In this paper the generator is only represented by a linear damper. This indicates $k_c = 0$. The non-dimensional CWR for the conventional WEC system is thus expressed as:

$$CWR = \frac{P}{P_{reg}L_e} = \frac{|H_{e\eta}(\omega)|^2}{\rho g c_g L_e} \frac{c_c\omega^2}{(k_w - M(\omega)\omega^2)^2 + \omega^2(C_h(\omega) + c_c)^2} \quad (18)$$

The optimal damping coefficient c_c can be obtained through optimizing Eq. (18) with respect to c_c , i.e., $\frac{\partial CWR}{\partial c_c} = 0$, resulting in:

$$c_c = \sqrt{C_h^2(\omega) + \frac{(k_w - M(\omega)\omega^2)^2}{\omega^2}} \quad (19)$$

In order to derive the upper limit of the absorbed mechanical power under monochromatic wave excitation as the benchmark, the control force consisting of mass, damping and stiffness terms is written as:

$$f_c(t) = m_c\ddot{u}(t) + c_c\dot{u}(t) + k_c u(t) \quad (20)$$

The time average power P_0 in this case becomes:

$$P_0 = \frac{1}{2}|F_e(\omega)|^2 \frac{\omega^2 c_c}{(k_w + k_c - \omega^2(m + M_h(\omega) + m_c))^2 + \omega^2(C_h + c_c)^2} \quad (21)$$

Maximization of P_0 with respect to m_c , c_c and k_c provides the optimal conditions, given as:

$$\left. \begin{aligned} k_c - \omega^2 m_c &= -k + \omega^2(m + M_h(\omega)) \\ c_c &= C_h(\omega) \end{aligned} \right\} \quad (22)$$

Finally, the optimal time-averaged power absorbed $P_{0,opt}$ is obtained as (Nielsen et al., 2013):

$$P_{0,opt} = \frac{1}{8} \frac{|F_e(\omega)|^2}{C_h(\omega)} \quad (23)$$

4. Inerter-based point absorber (IPA) WEC: closed-form optimization

As shown in Fig. 2(b), the parameters of the IPA WEC to be optimized are the damping coefficient and stiffness coefficient of the PTO system c_c and k_c , the stiffness coefficient k_2 of the connection springs and the inertance m_2 of the inerter. Assuming the mass moment of inertia of the flywheel to be J and the radius of the pulley to be r_p , the inertance m_2 turns out to be $m_2 = \frac{J}{r_p^2}$, based on the no-slip kinematical constrain between the translational motion and the rotational motion.

The IPA WEC system becomes a 2-DOF system because of the inclusion of the inerter and the connecting spring. The equation of motion is written as:

$$\begin{aligned} \begin{bmatrix} m + m_h & 0 \\ 0 & m_2 \end{bmatrix} \begin{bmatrix} \ddot{u}(t) \\ \ddot{u}_2(t) \end{bmatrix} + \begin{bmatrix} k_2 + k_w & -k_2 \\ -k_2 & k_2 \end{bmatrix} \begin{bmatrix} u(t) \\ u_2(t) \end{bmatrix} + \begin{bmatrix} \int_0^t h_{ru}(t-\tau)\dot{u}(\tau)d\tau \\ c_c\dot{u}_2(t) \end{bmatrix} \\ = \begin{bmatrix} f_e(t) \\ 0 \end{bmatrix} \end{aligned} \quad (24)$$

where $u(t)$ denotes the heave displacement of the float, while $u_2(t)$ denotes the displacement of the inerter with respect to the fixed structure. $u(t)$ and $u_2(t)$ make up the 2 DOFs of the system. Similar to the CPA WEC model, k_c for the generator of the IPA WEC model has been assumed to be zero in the following optimization. Note that for the IPA WEC, the generated power from the PTO system is now directly related to the inerter motion $u_2(t)$, rather than the float motion $u(t)$.

For monochromatic wave excitation, the equation of motion Eq. (24) can be simplified as:

$$\begin{aligned} \begin{bmatrix} M(\omega) & 0 \\ 0 & m_2 \end{bmatrix} \begin{bmatrix} \ddot{u}(t) \\ \ddot{u}_2(t) \end{bmatrix} + \begin{bmatrix} k_2 + k_w & -k_2 \\ -k_2 & k_2 \end{bmatrix} \begin{bmatrix} u(t) \\ u_2(t) \end{bmatrix} + \begin{bmatrix} C_h(\omega) & 0 \\ 0 & c_c \end{bmatrix} \begin{bmatrix} \dot{u}(t) \\ \dot{u}_2(t) \end{bmatrix} \\ = \begin{bmatrix} F_e(\omega)\cos(\omega t) \\ 0 \end{bmatrix} \end{aligned} \quad (25)$$

Eq. (25) in the frequency domain can be derived as:

$$\begin{bmatrix} k_2 + k_w - M(\omega)\omega^2 + iC_h(\omega)\omega & -k_2 \\ -k_2 & k_2 - m_2\omega^2 + ic_c\omega \end{bmatrix} \begin{bmatrix} U \\ U_2 \end{bmatrix} = \begin{bmatrix} F_e(\omega) \\ 0 \end{bmatrix} \quad (26)$$

Therefore, the complex harmonic response amplitudes $U(i\omega)$ and $U_2(i\omega)$ for the float and the inerter respectively can be obtained by solving Eq. (26), and are given as:

$$U(i\omega) = \frac{F_e(\omega)(k_2 - m_2\omega^2 + ic_c\omega)}{(k_2 + k_w - M(\omega)\omega^2 + iC_h(\omega)\omega)(k_2 - m_2\omega^2 + ic_c\omega) - k_2^2} \quad (27)$$

$$U_2(i\omega) = \frac{F_e(\omega)k_2}{(k_2 + k_w - M(\omega)\omega^2 + iC_h(\omega)\omega)(k_2 - m_2\omega^2 + ic_c\omega) - k_2^2} \quad (28)$$

Then, the frequency-domain transfer function $H_U(i\omega)$ (or $H_{U_2}(i\omega)$) between $U(i\omega)$ (or $U_2(i\omega)$) and the wave height H can be obtained as follows:

$$\begin{aligned} H_U(i\omega) &= \frac{U(i\omega)}{H} \\ &= \frac{1}{2} \frac{H_{e\eta}(\omega)(k_2 - m_2\omega^2 + ic_c\omega)}{(k_2 + k_w - M(\omega)\omega^2 + iC_h(\omega)\omega)(k_2 - m_2\omega^2 + ic_c\omega) - k_2^2} \end{aligned} \quad (29)$$

$$H_{U_2}(i\omega) = \frac{U_2(i\omega)}{H} = \frac{1}{2} \frac{H_{e\eta}(\omega)k_2}{(k_2 + k_w - M(\omega)\omega^2 + iC_h(\omega)\omega)(k_2 - m_2\omega^2 + ic_c\omega) - k_2^2} \quad (30)$$

whose amplitude (modulus) $|H_U(i\omega)|$ and $|H_{U_2}(i\omega)|$ can be regarded as the normalized response amplitudes of the float and the inerter, respectively.

The time-averaged power absorbed through the PTO system in Fig. 2(b) becomes:

$$P = \frac{1}{2} c_c |U_2|^2 \omega^2 \quad (31)$$

Insertion of Eq. (28) into Eq. (31) provides:

$$P = \frac{1}{2} |F_e(\omega)|^2 \frac{c_c k_2^2 \omega^2}{(k_2^2 + C_h(\omega)c_c\omega^2 - AB)^2 + \omega^2(C_h(\omega)A + c_c B)^2} \quad (32)$$

where

$$A = k_2 - m_2\omega^2, \quad B = k_2 + k_w - M(\omega)\omega^2 \quad (33)$$

Then, the non-dimensional CWR for the IPA WEC can be expressed as:

$$CWR = \frac{P}{P_{reg} L_e} = \frac{|H_{e\eta}^2(\omega)|}{\rho g c_g(\omega) L_e} \times \frac{c_c k_2^2 \omega^2}{(k_2^2 + C_h(\omega)c_c\omega^2 - AB)^2 + \omega^2(C_h(\omega)A + c_c B)^2} \quad (34)$$

From Eq. (34) it is seen that the CWR is a function of the inertance m_2 , connecting stiffness k_2 and damping coefficient c_c . The partial derivatives of CWR with respect to c_c , m_2 and k_2 provide the optimal $m_{2,opt}$, $k_{2,opt}$ and $c_{c,opt}$, given as:

$$m_{2,opt} = \frac{\omega^2 C_h^2(\omega) k_{2,opt} + k_{2,opt} (k_w - M(\omega)\omega^2) (k_{2,opt} + k_w - M(\omega)\omega^2)}{\omega^2 (k_{2,opt} + k_w - M(\omega)\omega^2)^2 + C_h^2(\omega) \omega^4} \quad (35)$$

$$k_{2,opt} = \frac{\omega^2 (C_h c_{c,opt} + k_w m_{2,opt} - m_{2,opt} M(\omega)\omega^2)^2 + (c_{c,opt} (k_w - M(\omega)\omega^2) - C_h m_{2,opt} \omega^2)^2}{- (C_h + c_{c,opt}) (c_{c,opt} (k_w - M(\omega)\omega^2) - C_h m_{2,opt} \omega^2) + (k_w - M(\omega)\omega^2 - m_{2,opt} \omega^2) (C_h c_{c,opt} + k_w m_{2,opt} - m_{2,opt} M(\omega)\omega^2)} \quad (36)$$

$$c_{c,opt} = \sqrt{\frac{(k_{2,opt}^2 - (k_{2,opt} - m_{2,opt} \omega^2)(k_{2,opt} + k_w - M(\omega)\omega^2))^2 + \omega^2 C_h^2(\omega) (k_{2,opt} - m_{2,opt} \omega^2)^2}{C_h^2(\omega) \omega^4 + \omega^2 (k_{2,opt} + k_w - M(\omega)\omega^2)^2}} \quad (37)$$

It can be seen that $k_{2,opt}$, $m_{2,opt}$ and $c_{c,opt}$ are fully coupled in Eqs. (36) and (37), whereas only $k_{2,opt}$, $m_{2,opt}$ are mutually coupled in Eq. (35). This means that the other two parameters can be determined for a given initial $k_{2,0}$. Insertion of the obtained $m_{2,opt}$ and $c_{c,opt}$ for a given $k_{2,0}$ into Eq. (35) provides the result of k_2 to be compared with the given initial $k_{2,0}$, which can be used to check if Eq. (35) holds automatically. This procedure will be validated in the subsequent section.

5. Performance evaluation of the WECs under regular waves

The heave point absorber in Fig. 3 (Sun and Nielsen, 2018) is used in the following numerical example for performance evaluation of the two WECs discussed above. It is formed with a cylinder with a diameter $D = 14.0$ m and draft depth $H = 7.0$ m connected to a hemisphere at the bottom with the same diameter as the cylinder. The mass of the float m is 1.84×10^6 kg and the stiffness k_w due to the hydrostatic

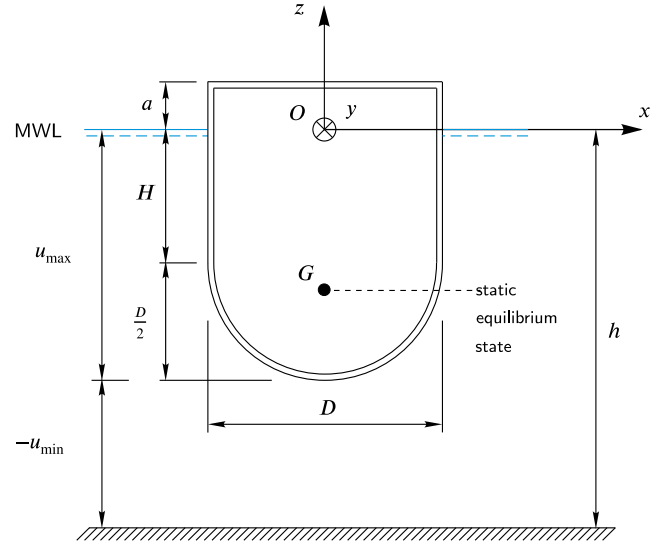


Fig. 3. Geometry of the heave point absorber.

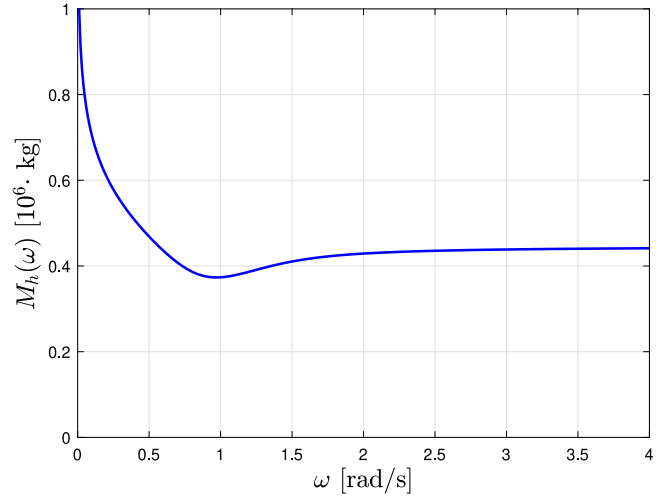


Fig. 4. Hydrodynamic added mass.

buoyancy is 1.55×10^6 N/m. Furthermore, the height over mean water level (MWL) for the cylinder is $a = 8.0$ m. The water depth h considered is 30 m. In application, the point absorber can neither jumper out of the water nor hit the sea bed. That means the point absorber must move in the constrained range between u_{max} and u_{min} given in Fig. 3. WAMIT (Lee and Newman, 2006) is applied to model the interaction between the wave and the PA WEC, from which the hydrodynamic parameters $M_h(\omega)$, $H_{ru}(\omega)$, $H_{e\eta}(\omega)$ are numerically obtained and the added mass at infinite frequency m_h is 0.44×10^6 kg. The hydrodynamic added mass is shown in Fig. 4. Figs. 5 and 6 illustrate the frequency response functions with real parts and imaginary parts for the radiation force and the excitation force, respectively.

In order to compare the performance of the IPA WEC with the CPA WEC in terms of the power conversion efficiency (CWR) as well as the frequency responses, three different control strategies for the IPA WEC have been considered: (1) IPA with active control where all parameters vary with the wave excitation frequency; (2) IPA with hybrid control where some parameters vary with the wave frequency and the rest are kept constant; (3) IPA with passive control where all parameters are constant. Each of them will be detailed in the subsequent sections.

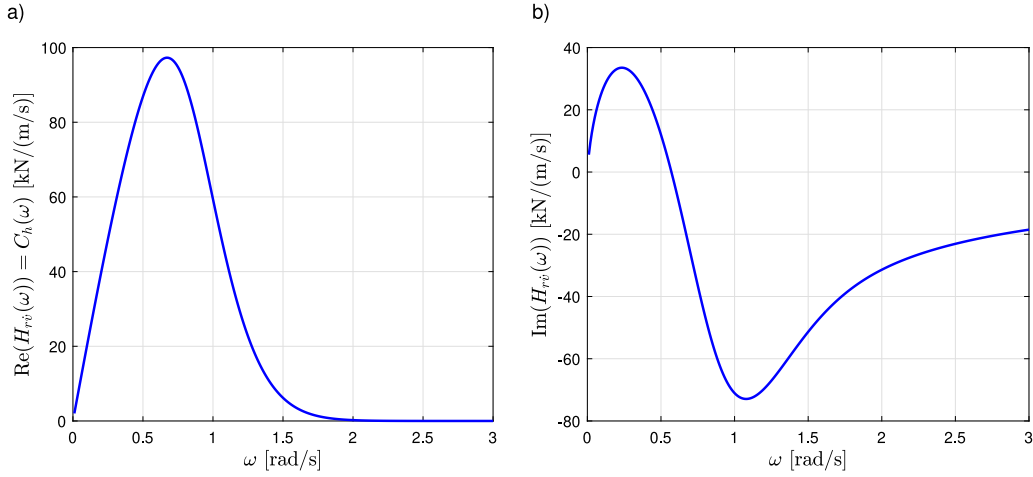


Fig. 5. Frequency response function of the radiation force. (a) Real part $\text{Re}(H_{rv}(\omega))$. (b) Imaginary part $\text{Im}(H_{rv}(\omega))$.

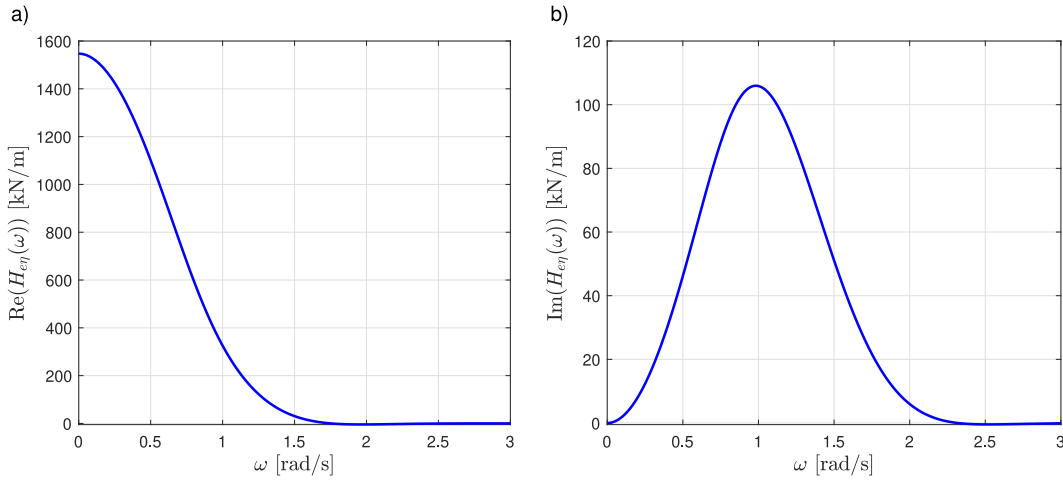


Fig. 6. Frequency response function of the wave excitation force. (a) Real part $\text{Re}(H_{ev}(\omega))$. (b) Imaginary part $\text{Im}(H_{ev}(\omega))$.

5.1. IPA with active control

To apply the proposed theory in Eqs. (35)–(37), the initial $k_{2,0}$ needs to be chosen first due to the coupling of c_c , k_2 and m_2 . Given an initial value of $k_{2,0} = 0.05k_w$, it turns out that the optimal condition Eq. (36) holds automatically as seen in Fig. 7(a), as long as m_2 and c_c have been determined by Eqs. (35) and (37), respectively. Fig. 7(b) shows the optimal CWR of the IPA with active control in comparison to that of the CPA with optimal damping control (c_c varies with the wave frequency). It can be found that the CWR curve for the IPA with active control is identical to the result for the CPA under full active control (Eq. (20)) (Nielsen et al., 2013). Those two CWR curves are aligned with the theoretical optimal CWR for a point absorber WEC representing the upper limit of power absorption, which is a constant with varying wave excitation frequencies, given as $1/2\pi$ (Falnes and Kurniawan, 2020). Furthermore, the IPA with active control significantly outperforms the CPA with optimal damping control. This indicates that the operational bandwidth and the absorbed power magnitude for the proposed system are significantly increased especially for the wave frequency away from the float resonance frequency, due to the introduction of the tuning inerter-spring system. The related parameters k_2 , c_c and m_2 with respect to ω are illustrated in Fig. 7(a), which have been normalized by k_w , $\max(C_h)$ and m respectively. As seen, the inertance m_2 must be large enough in order to keep the IPA system resonate with the wave excitation at low frequencies. When

the wave excitation frequency increases, m_2 decreases until the wave frequency is aligned with a specific frequency, approximately given as $\omega_a = 0.84$ rad/s that is close to the float natural frequency of the CPA, given as $\omega_f = \sqrt{k_w/(m+m_h)} = 0.82$ rad/s. For a short interval of wave frequencies after ω_a , up to approximately $\omega_b = 0.87$ rad/s, the inertance m_2 increases drastically. After ω_b , m_2 gradually decreases again to keep the IPA system in resonance to maximize the absorbed power. This can be further observed in the two modal frequencies of the IPA system as given in Fig. 7(e) where ω_1 and ω_2 represent the first and second modal frequencies of this 2-DOF system. As seen, the IPA resonates at the first modal frequency ω_1 for wave frequencies below ω_a , while the resonance of the proposed system switches to the second modal frequency ω_2 for wave frequencies over ω_b . For a short frequency interval from ω_a to ω_b , the wave frequency is located between the two modal frequencies. In this interval, although neither of the modal frequencies is aligned with the wave frequency, the IPA system still performs optimally as seen in Fig. 7(b). Actually, here the IPA is in double-mode response, similar to the case of a structure-TMD system (Krenk, 2005; Zhang, 2020) when the excitation frequency is close to the natural frequency of uncontrolled structure (corresponding to the float here). Furthermore, the resonance switching between ω_1 and ω_2 increases the potential of broadening the operational bandwidth and improving power absorption. Fig. 7(c) and (d) demonstrate the absolute amplitudes of the float $|H_U|$ and the inerter $|H_{U_2}|$ under active

control respectively. As expected, the amplitude of float in the active-controlled IPA is equal to the theoretical optimal and it is significantly larger than the CPA when ω is away from the narrow resonance bandwidth of the float. Furthermore, the inerter amplitude is significantly amplified in comparison to the float response, especially for wave frequencies outside the interval $[\omega_a, \omega_b]$. This phenomenon is caused by the inclusion of the tuning spring k_2 , implying that the inerter-spring system contributes to the IPA resonance when ω is outside the above-mentioned frequency interval.

To investigate the effect of $k_{2,0}$ on the optimal CWR curve and the frequency responses for float and inerter, as well as parameters c_c and m_2 , another initial value of $k_{2,0} = 0.08k_w$ is considered. The comparisons in Fig. 7(b) and (c) reveal that the optimal CWR curve and float response are independent on the chosen initial $k_{2,0}$. On the other hand, as seen from Fig. 7(a) and (d), c_c , m_2 and the inerter response is dependent on the initial value $k_{2,0}$ while maintaining the similar change trend respectively. Therefore, it can be concluded that $k_{2,0}$ does not change the WEC response and the optimal power output under active control, and merely influences the other system parameters and the inerter response.

5.2. IPA with hybrid control

This subsection deals with the IPA with hybrid control strategies where one or two out of the three parameters are fixed. Three different configurations of the hybrid control strategies are considered: (1) IPA hybrid control 1 where c_c is fixed while k_2 and m_2 vary with ω ; (2) IPA hybrid control 2 where c_c and k_2 are fixed while m_2 varies with ω ; (3) IPA hybrid control 3 where m_2 and k_2 are fixed while c_c varies with ω . The initial value of $k_{2,0} = 0.05k_w$ is used. For hybrid control strategies 1 and 2 where c_c is fixed, the corresponding passive CPA system (with fixed c_c) is also considered for comparison. On the other hand, for hybrid control strategy 3, the corresponding CPA with active damping control is evaluated for comparison.

5.2.1. IPA hybrid control 1

Given the parameter c_c , the corresponding k_2 and m_2 can be obtained iteratively using Eqs. (35) and (36). The detailed procedure is: (1) Calculating m_2 using the given initial $k_{2,0}$. (2) Determining k_2 using the given c_c and the aforementioned m_2 . (3) Calculating m_2 and k_2 iteratively. Fig. 8(a) shows the CWR curve as a function of the iteration number n with $c_c = 0.2 \max(C_h)$. As seen, the CWR curve will gradually approach the theoretical solution as the iteration number n increases. In practice, only wave excitation frequencies with a certain range is of interest, and thus a design frequency interval where the device operates optimally should be specified for hybrid control. Compared to the result for active control in Fig. 7(b), IPA hybrid control 1 can achieve optimal performance for this specified design frequency interval, not for all wave frequencies. The iteration number $n = 50$ is chosen in the subsequent analysis, resulting in the design frequency interval shown in the red curve in Fig. 8(a). CWR comparison between hybrid control 1 and active control of the IPA shows that the damping plays an important role on the energy absorption for wave frequencies outside the specified design frequency interval, although the proposed system can in principle be tuned to be in resonance by varying the parameters k_2 and m_2 . Fig. 8(b) shows the CWR comparison between the IPA hybrid control 1 (with the damping coefficient $c_c = 0.2 \max(C_h)$) and the CPA passive control (with the same c_c). To investigate the effect of c_c on the IPA, another $c_c = 0.5 \max(C_h)$ is also considered. The IPA hybrid control 1 significantly outperforms the CPA passive control, in terms of the larger value of CWR and a much broader curve. The related parameters k_2 and m_2 with respect to ω are illustrated in Fig. 8(c). As seen, the variation of the inertance m_2 follows the trend of the active control case given in Fig. 7(a), especially for the specified design frequency interval (wave frequencies where the optimal device performance is guaranteed). Outside the specified design frequency interval, the tuning

spring k_2 exhibits an increasing trend, respectively. Within the specified design frequency interval, k_2 exhibits the same variational trend as m_2 , maintaining the IPA system in resonance with the incoming wave to perform optimally.

Fig. 8(f) shows the variation of modal frequencies ω_1 and ω_2 of the IPA system with respect to wave frequency ω . It can be seen that ω_1 and ω_2 follow a similar variational trend as the active control case in Fig. 7(e). The corresponding normalized response amplitudes of float $|H_U|$ and inerter $|H_{U_2}|$ are given in Fig. 8(d) and (e), respectively. Except for wave frequencies close to the float natural frequency of the CPA, ω_f , the float response amplitude of IPA is always larger than that of the CPA float. This indicates the increased potential of extracting more energy from waves. Comparison between Fig. 8(d) and (e) shows that the inerter response amplitude is significantly amplified in comparison with the float response for the IPA system, especially at small wave frequencies.

5.2.2. IPA hybrid control 2

The IPA hybrid control 2 is a variation of the IPA hybrid control 1. c_c and k_2 are fixed, and only m_2 varies with ω . Fig. 9 shows the results for the IPA hybrid control 2 with $c_c = 0.2 \max(C_h)$ and $k_2 = 0.05k_w$. The CWR curve is compared with those of the IPA hybrid control 1 and CPA passive control, as shown in Fig. 9(a). The IPA hybrid control 2 falls behind the IPA hybrid control 1 as expected, and the performance reduction can reflect the importance of the tuning spring k_2 on the device performance in terms of the energy absorption and the operational bandwidth. Furthermore, IPA hybrid control 2 can significantly outperform the CPA passive control although there is a local minimum in CWR curve due to the fixed k_2 . This local minimum, together with the two local maximums, represent the characteristic of a 2-DOF system to some extent. The corresponding variation of m_2 is given in Fig. 9(b), which is determined merely based on the given k_2 . Fig. 9(c) demonstrates the response amplitude comparison between the two systems. The float response of the IPA is smaller than that of CPA at wave frequencies close to ω_f , and the response of inerter is significantly larger than the float responses of IPA and CPA, especially for wave frequencies far away from ω_f . This indicates that IPA hybrid control 2 only with varying inertance m_2 can not only improve the energy absorption and broaden the operational bandwidth, but also reduce the float amplitude close to ω_f comparing with passive CPA. This is beneficial to the fatigue life of the float. The variation of ω_1 and ω_2 shown in Fig. 9(e) can reflect the variation of the two modal frequencies of the IPA system with the wave frequency by actively tuning m_2 . A similar trend is observed as in Figs. 7(e) and 8(f).

Fig. 10 shows the results of the IPA hybrid control 2 with a new value of c_c ($c_c = 0.5 \max(C_h)$) and $k_2 = 0.05k_w$. The CPA passive control with the same new c_c value ($c_c = 0.5 \max(C_h)$) is also evaluated for comparison. The CWR curve for the passive CPA with $c_c = 0.5 \max(C_h)$ is closer to the theoretical solution for wave frequencies close to the float natural frequency ω_f , compared with the result for $c_c = 0.2 \max(C_h)$. Nevertheless, the IPA hybrid control 2 still outperforms the CPA passive control with larger CWR values and a broader operational bandwidth. The corresponding m_2 is identical to that for $c_c = 0.2 \max(C_h)$ given in Fig. 10(b) because m_2 is merely determined by k_2 . The related $|H_U|$, $|H_{U_2}|$ are illustrated in Fig. 10(b). As seen, the same conclusion for the case with $c_c = 0.2 \max(C_h)$ is applied to the case with $c_c = 0.5 \max(C_h)$. Furthermore, the response amplitude of the inerter in the IPA is of similar magnitudes with the float response in the CPA for wave frequencies close to ω_f , implying a more close performance between IPA and CPA in this case comparing with that in Fig. 9. Therefore, comparison of the two cases with different values of c_c indicates that the damping coefficient c_c plays an important role in determining the extent to which the performance of the IPA hybrid control 2 is improved comparing with CPA passive control.

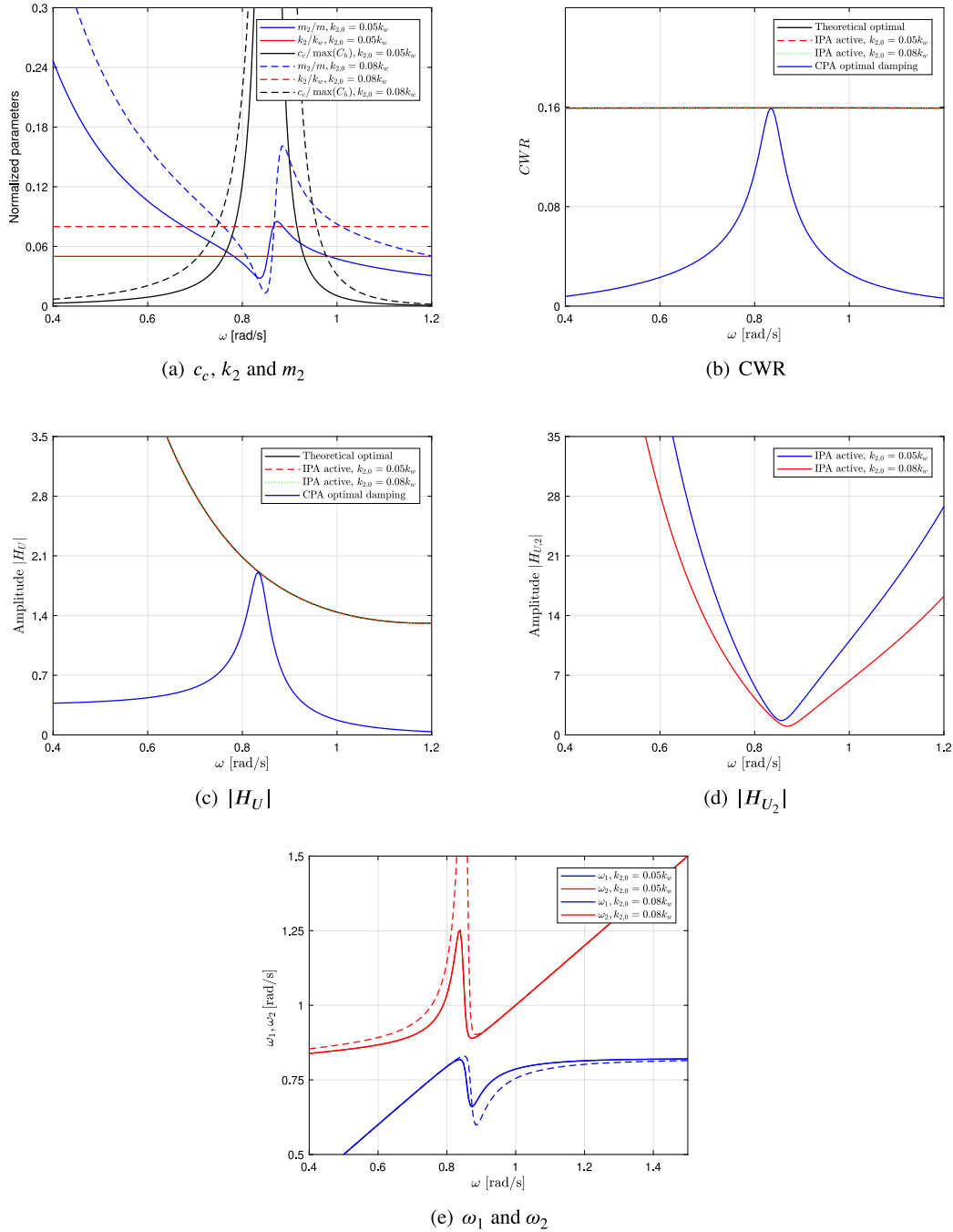


Fig. 7. IPA active control in comparison with CPA optimal damping control.

5.2.3. IPA hybrid control 3

IPA hybrid control 3 is investigated in this subsection where $m_2 = 0.06$ m, $k_2 = 0.05k_w$ are chosen and c_c varies with respect to ω . In this case, the undamped eigenfrequencies of the 2-DOF system (the float in series with the inerter) are invariant with respect to ω , i.e. $\omega_1 = 0.75$ rad/s and $\omega_2 = 0.94$ rad/s. The CWR comparison between IPA hybrid control 3 and CPA optimal damping control is shown in Fig. 11(a). The result indicates that the operational bandwidth for the IPA hybrid control 3 is broader than the CPA optimal damping control, although the magnitude of CWR for the IPA is lower than that for the CPA for a narrow range of wave frequencies. The corresponding optimal c_c for IPA hybrid control 3 is generally much smaller than that for CPA optimal damping control as seen from Fig. 11(b). This

can be reflected based on the comparison between Eqs. (19) and (37) that given the parameters k_2 and m_2 , the damping coefficient c_c in Eq. (19) positively correlates with $C_h(\omega)$ while the damping coefficient c_c in Eq. (37) presents positive correlation with the reciprocal of $C_h(\omega)$.

Fig. 11(c) shows that the float response of the IPA has similar magnitudes as that of the CPA. On the other hand, the inerter response of the IPA is significantly amplified, especially for wave excitation frequencies away from the float natural frequency ω_f . The two large peaks of the inerter response amplitude correspond to the two peaks of the CWR curve in Fig. 11(a), indicating that at these two wave frequencies the inerter is significantly excited to realize optimal power extraction.

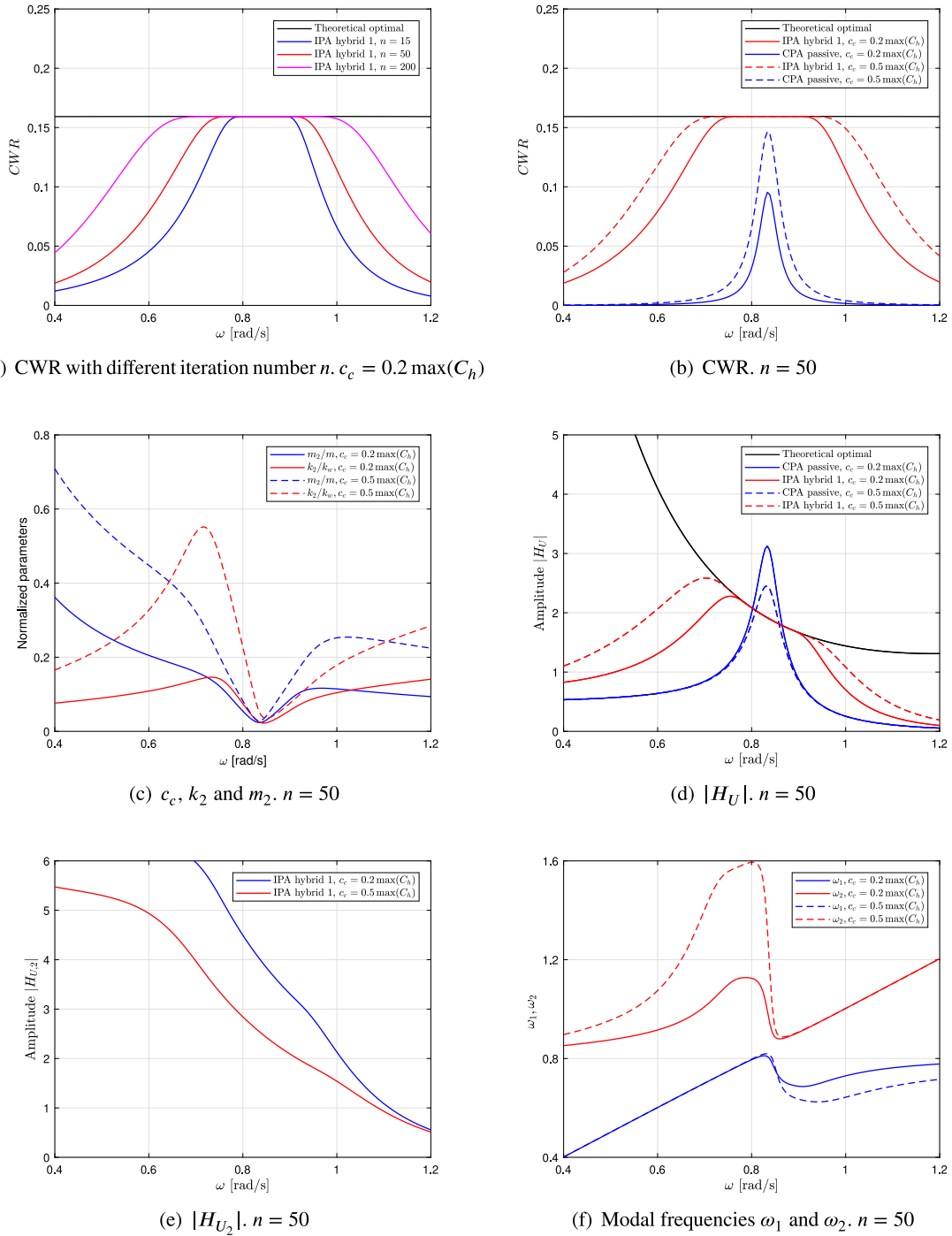


Fig. 8. IPA hybrid control 1 in comparison with CPA passive control. $k_{2,0} = 0.05k_w$. (For interpretation of the references to color in this figure legend, the reader is referred to the web version of this article.)

5.3. IPA with passive control

In this subsection, performance of the IPA system with passive control is compared with that of the passive CPA. The parameters k_2 and m_2 are chosen based on the result from the IPA hybrid control 1 illustrated in Fig. 8(c). Fig. 12(a) compares the CWR curves of the passive IPA and the passive CPA with the same $c_c = 0.2 \max(C_h)$, where the chosen $k_2 = 0.0238k_w$ and $m_2 = 0.0238$ m have been determined using the minimal intersection point of k_2 and m_2 corresponding to wave excitation frequency $\omega = 0.837$ rad/s in Fig. 8(c). As seen, the passive IPA can absorb more power than the passive CPA and presents broader operational bandwidth. Furthermore, the modal frequencies

of the 2-DOF IPA system for this case are 0.79 rad/s and 0.95 rad/s, and the CWR curve achieves the theoretical optimum at the frequency close to ω_f (0.82 rad/s), e.g. the natural frequency of float solely. Fig. 12(b) compares the corresponding float response amplitudes of the two systems as well as the inerter response of the IPA. It is observed that the float response amplitude for the IPA system is reduced while the response amplitude of the inerter is amplified, implying that the mechanical energy is transferred from the float to the inerter.

Fig. 12(c) shows the CWR curve of the passive IPA with a different set of values of k_2 and m_2 . Here the parameters $k_2 = 0.0335k_w$ and $m_2 = 0.0508$ m corresponding to wave excitation frequency $\omega = 0.87$ rad/s in Fig. 8(c) have been chosen. It can again be observed that the effective

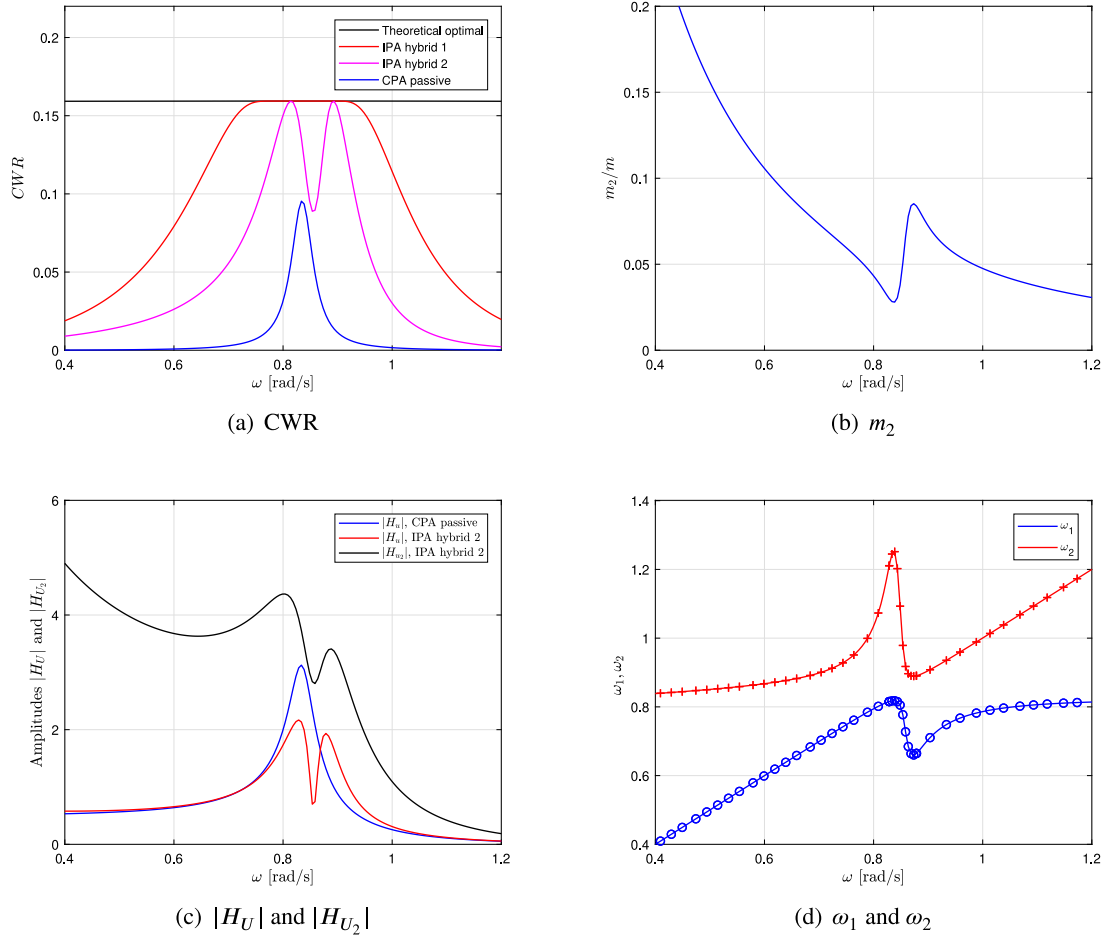


Fig. 9. IPA hybrid control 2 in comparison with CPA passive control. $c_c = 0.2 \max(C_h)$. $k_2 = 0.05 k_w$.

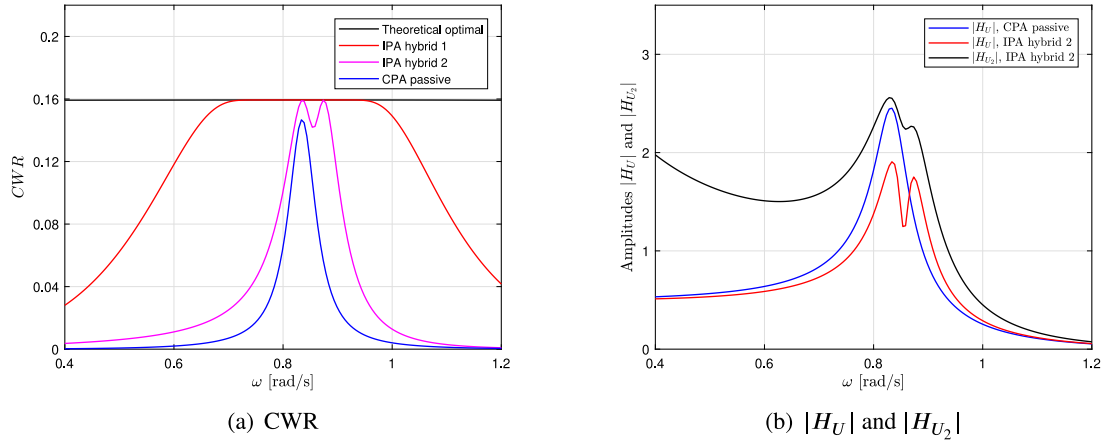


Fig. 10. IPA hybrid control 2 in comparison with CPA passive control. $c_c = 0.5 \max(C_h)$. $k_2 = 0.05 k_w$.

frequency bandwidth of this passive IPA is much broader than that of the passive CPA, and is even broader than the case given in Fig. 8(a). Furthermore, the two modal frequencies for this case are 0.70 rad/s and 0.87 rad/s. It can be observed that when the wave excitation frequency is aligned with the second modal frequency, the CWR curve reaches the theoretical optimum, as shown in Fig. 12(c). This is due to the fact that the second modal frequency in this case is more close to ω_f (0.82 rad/s). Fig. 12(d) demonstrates the corresponding response amplitudes related to the floats and the inerter. Similarly, the IPA float response is significantly smaller than the CPA float response at

frequencies close to ω_f , and the IPA inerter response is significantly amplified. Furthermore, comparison between two cases with different parameter sets of k_2 and m_2 shows that the chosen of proper parameter set of k_2 and m_2 can lead to better operational bandwidth for the passive IPA system.

Fig. 13(a) shows the CWR curve comparison between the passive IPA and passive CPA where another value of c_c , $c_c = 0.5 \max(C_h)$, has been used. The values of $m_2 = 0.0362$ m and $k_2 = 0.0362 k_w$ corresponding to $\omega = 0.846$ rad/s in Fig. 8(c) have been obtained following the same rule, i.e. the minimal intersection point of k_2 and

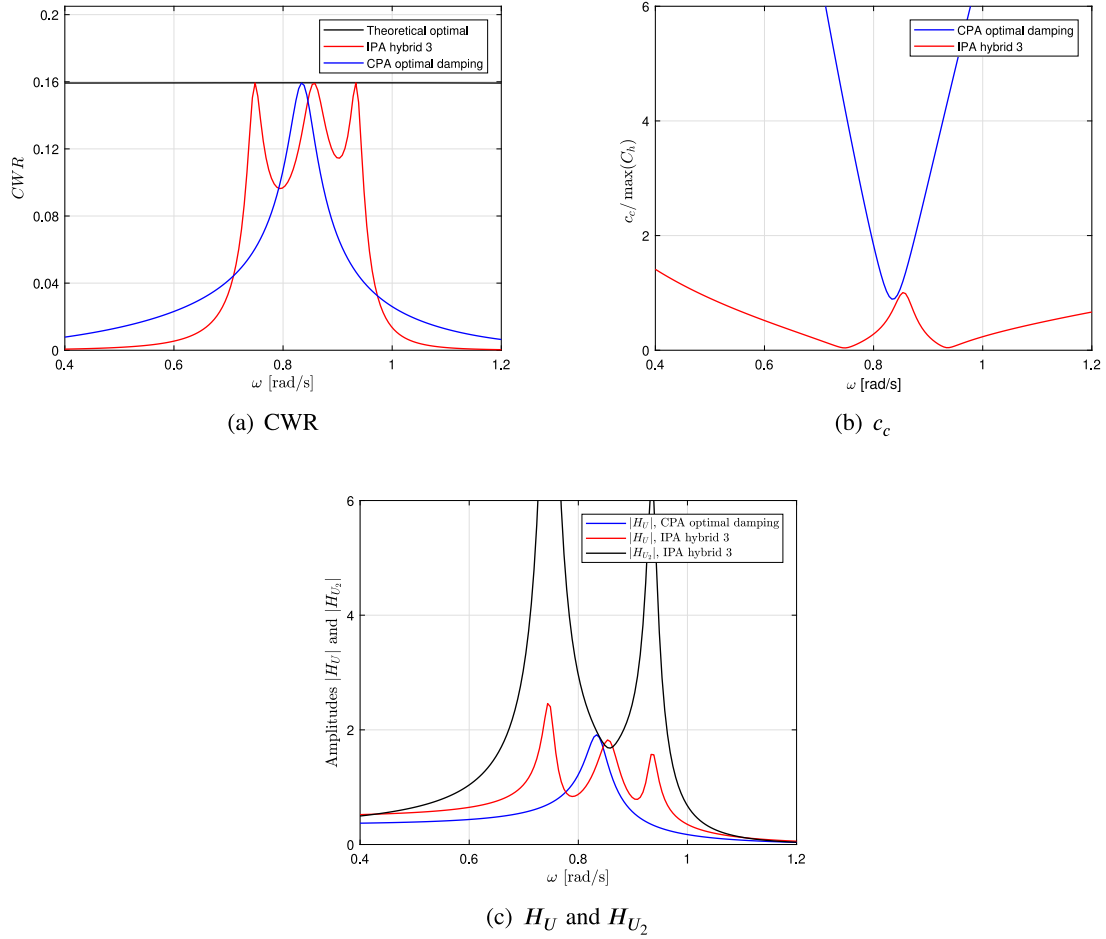


Fig. 11. IPA hybrid control 3 in comparison with CPA optimal damping control. $m_2 = 0.06$ m. $k_2 = 0.05k_w$.

m_2 for $c_c = 0.5 \max(C_h)$ has been chosen. Furthermore, the modal frequencies of the IPA system or this case are 0.78 rad/s and 0.97 rad/s. As seen, the improvement of IPA passive is not as significant as that for the case of $c_c = 0.2 \max(C_h)$ in Fig. 12(a). This is because the room to be improved by passive IPA is reduced compared to the case with $c_c = 0.2 \max(C_h)$, due to the proximity to the upper limit at frequencies close to ω_f for passive CPA with $c_c = 0.5 \max(C_h)$. The corresponding response amplitudes related to the floats and the inerter are shown in Fig. 13(b). Similar observations can be made as in Fig. 12(b), although the CPA float response curve is more close to the IPA inerter response curve implying the satisfactory performance of the passive CPA with $c_c = 0.5 \max(C_h)$.

6. Performance evaluation of the WECs under irregular waves

In this section, performance comparison of the proposed IPA and the CPA is carried out under irregular waves. JONSWAP wave spectrum (Hasselmann et al., 1973) with given significant wave height H_s and peak period T_p is employed to generate the wave excitation force, and time-domain simulations are subsequently performed using Eq. (24). Both narrowbanded and broadband stochastic wave excitation forces are considered, which are defined by the bandwidth parameter γ of the JONSWAP spectrum (Hasselmann et al., 1973). To have a realistic and practical scenario, only passive IPA and CPA WECs are considered in this section.

Basically, the performance of point absorber to be concerned is in a certain frequency interval because in practice the wave energy of interest is mainly distributed in a limited frequency range. For the point absorber considered here, the frequency band of interest around

the float natural frequency is chosen as [0.628 rad/s, 1.257 rad/s] corresponding to [5 s, 10 s] for period band. This means that the proposed IPA is designed to operate in resonant condition in the aforementioned frequency band. Then, the optimization of the passive IPA parameters k_2 , m_2 and c_c are conducted to maximize the power output from the irregular wave, with the constraint that the two modal frequencies of the resulting system should lie within [0.628 rad/s, 1.257 rad/s]. On the other hand, the CPA parameter c_c is optimized without constraints. Irregular sea states with different values of wave peak frequency ω_p and a fixed value of significant wave height $H_s = 2$ m are used in the following simulations.

Fig. 14 (a) and (b) show the numerically optimized CWR curves of both IPA and CPA with respect to the wave peak frequencies, for $\gamma = 1.0$ and $\gamma = 3.3$, respectively. For each sea state indicated by ω_p , a set of optimal parameters of the device have been uniquely determined. Therefore, for different ω_p the parameters of the passive devices are different. This means that the CWR curves in Fig. 14 are only of theoretical relevance. Nevertheless, the results in Fig. 14 reveal the inherently superior performance of the proposed IPA over CPA (when both are optimized), for all considered irregular sea states. Note that there are slope discontinuities in the optimal CWR curves for the IPA WEC. This is caused by the imposed constraint of modal frequencies of the IPA system during parametric optimization, as mentioned above.

It can be observed that the optimal passive IPA outperforms the optimal passive CPA in terms of energy absorption and operational bandwidth, especially for wave peak frequencies away from the float natural frequency ω_f . This is due to the fact that the CPA with a given float design can never operate in resonance when the wave peak frequencies shift away from ω_f , while the additional inerter-spring system

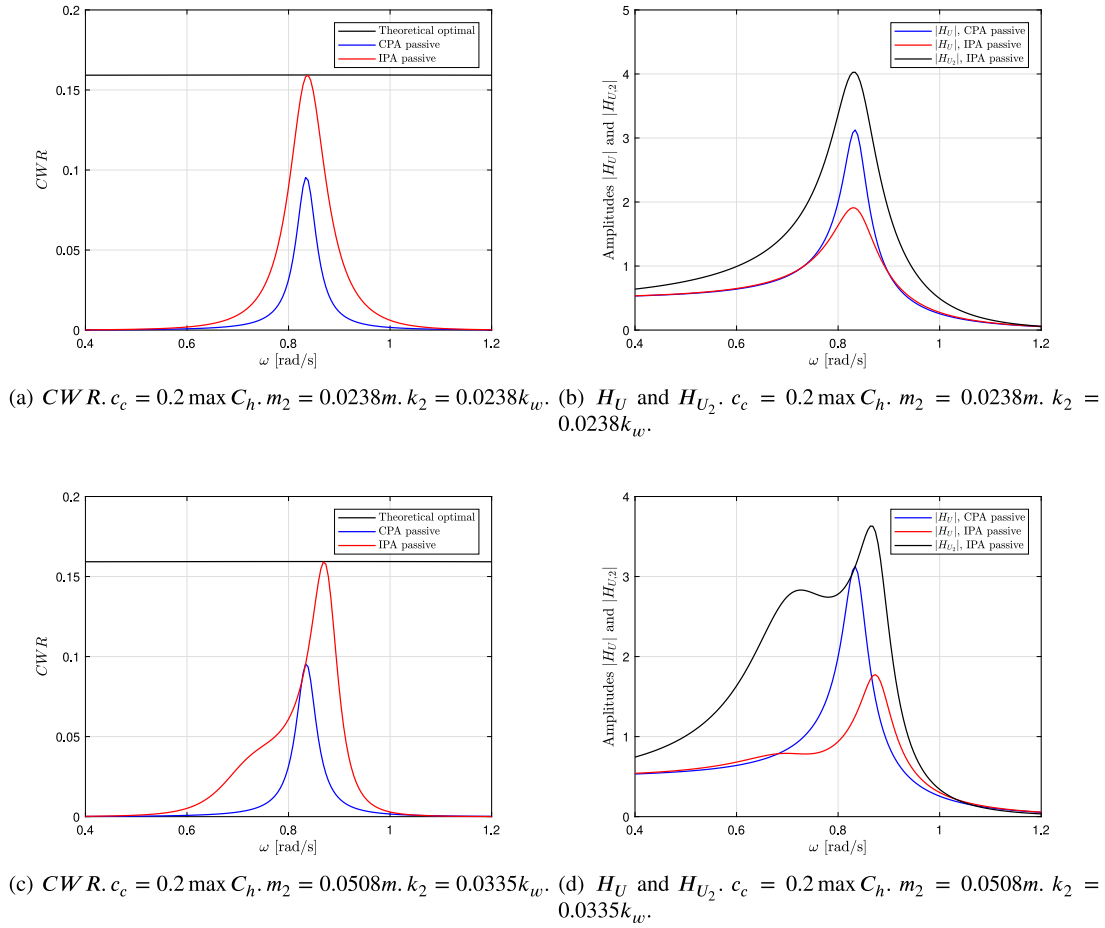
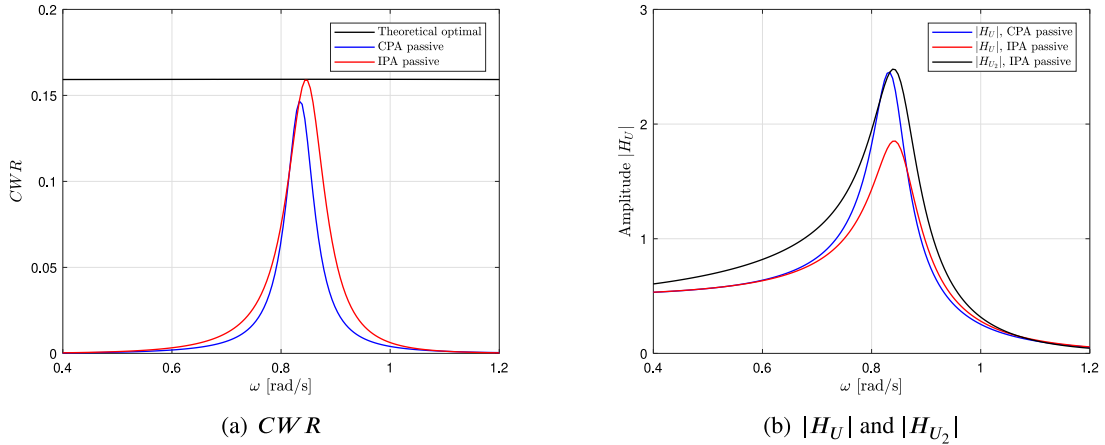


Fig. 12. IPA passive control in comparison with CPA passive control.

Fig. 13. IPA passive control in comparison with CPA passive control. $c_c = 0.5 \max C_h$. $m_2 = 0.0362m$. $k_2 = 0.0362k_w$.

of the IPA facilitates the frequency adaptation of the system so that the system can be in resonance in a broader wave frequency interval. To further quantify this mechanism, Table 1 shows the different sets of modal frequencies of the optimized IPA system for different sea states, i.e. $\omega_p = 0.683 \text{ rad/s}, 0.748 \text{ rad/s}, 0.873 \text{ rad/s}, 1.083 \text{ rad/s}$, with $\gamma = 1.0$. It can be observed that when the wave peak frequency ω_p is close to the float natural frequency ω_f , the optimized IPA system has two modal frequencies ω_1 and ω_2 such that ω_p is located between ω_1 and ω_2 . When ω_p is far smaller than ω_f , ω_1 of the optimized IPA system turns out to be close to ω_p leading to first-mode resonance with wave. Similarly,

second-mode resonance of the optimized IPA system is achieved when the wave frequency ω_p is far larger than ω_f , i.e. ω_2 turns out to be close to ω_p .

Next, Fig. 15 shows the CWR curves of the passive CPA and IPA WECs having fixed parameters, with respect to different sea states. $\gamma = 1.0$ is kept unchanged. The parameters of the CPA are optimized for $\omega_p = 0.873 \text{ rad/s}$, and are applied to all sea states (thus non-optimal for wave periods other than $\omega_p = 0.873 \text{ rad/s}$). As for the IPA, optimization has been performed for four discrete sea states, i.e. $\omega_p = 0.683 \text{ rad/s}, 0.748 \text{ rad/s}, 0.873 \text{ rad/s}, 1.083 \text{ rad/s}$, leading to four different

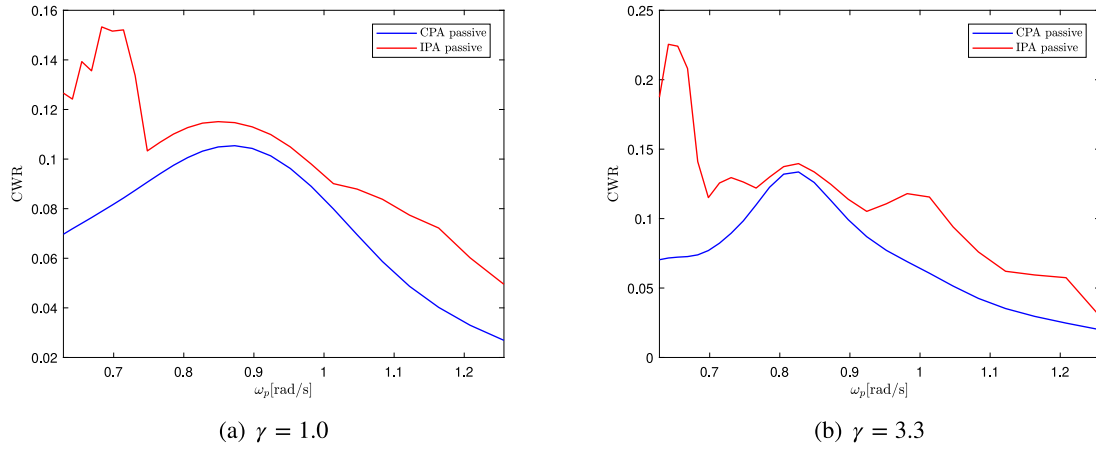


Fig. 14. Passive IPA WEC in comparison with passive CPA WEC. The WECs have been optimized for each sea state.

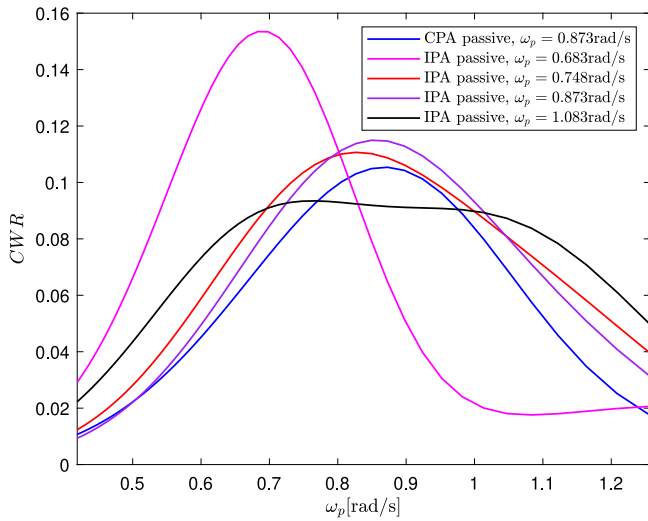


Fig. 15. IPA passive control in comparison with CPA passive control. Fixed IPA passive control is applied to all sea states. $\gamma = 1.0$.

Table 1

Modal periods of the 2-DOF IPA system (optimized) for different ω_p .

ω_1, ω_2 [rad/s]	ω_p [rad/s]			
	0.683	0.748	0.873	1.083
ω_1	0.640	0.710	0.738	0.628
ω_2	1.257	1.025	1.002	1.015

configurations of the passive IPA corresponding to the four curves in Fig. 15. The comparison of the CWR curves shows that all four configurations of the passive IPA perform better than the passive CPA. Different IPA configurations lead to different operational bandwidths and peaks of the curves, which indicates that different targeted wave excitation frequencies can be tackled by the IPA system through the optimization strategy. Furthermore, results in Table 1 and Fig. 15 indicate that increasing the interval between modal frequencies ω_1 and ω_2 can lead to broader operational bandwidth of the IPA system.

In order to practically demonstrate the efficacy of the passive IPA in irregular seas, sea states with $\omega_p = 0.873$ rad/s and $\omega_p = 0.683$ rad/s are chosen for time-domain simulations, corresponding to wave peak frequencies close to and far away to the float natural frequency ω_f , respectively. Fig. 16(a) and (b) illustrate the time series of wave excitation forces with $\omega_p = 0.873$ rad/s and $\omega_p = 0.683$ rad/s, respectively.

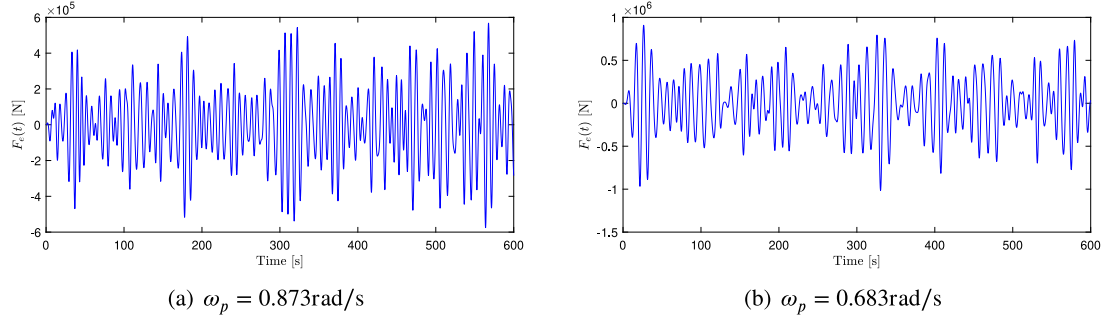
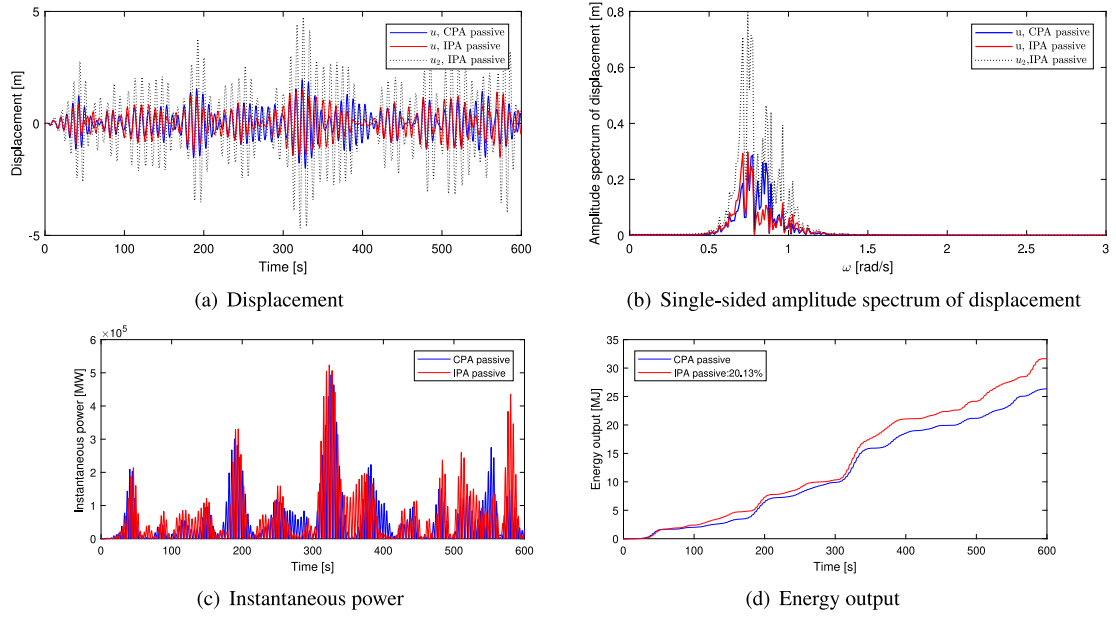
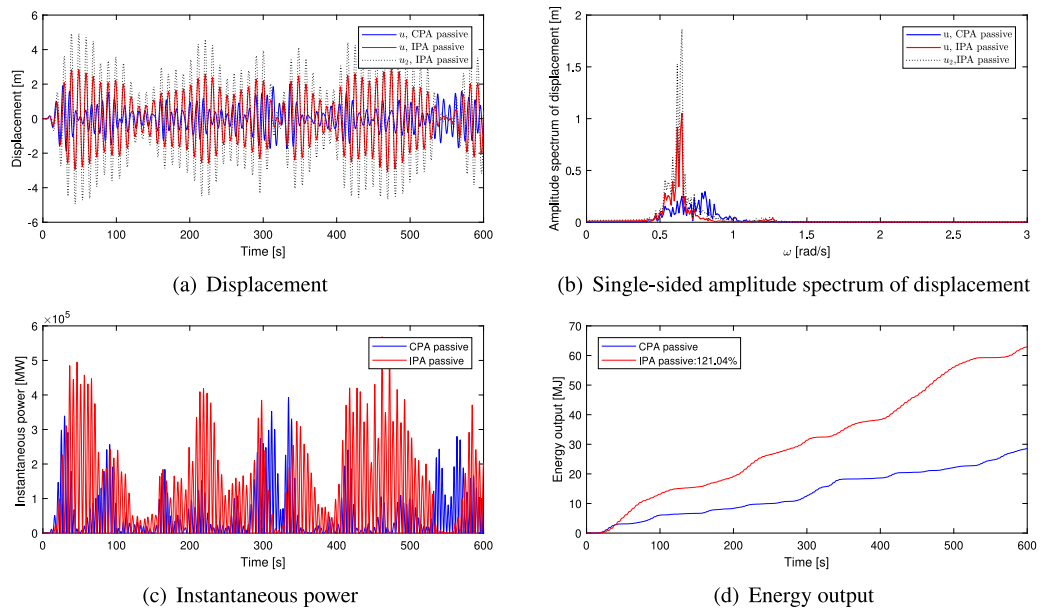
Fig. 17 shows the time series of the displacements of float and inerter, the instantaneous power and the energy output under the wave excitation with $\omega_p = 0.873$ rad/s. The single-sided Fourier amplitude spectra for float and inerter displacements are also compared in Fig. 17(b). Both the passive IPA and CPA have been optimized for $\omega_p = 0.873$ rad/s. It can be observed that the float response of the passive IPA is generally smaller than that of passive CPA while the inerter response is much larger than that of the floats. Furthermore, compared with the CPA float, the distribution of Fourier amplitude spectrum for the IPA float displacement becomes narrow, while the Fourier amplitude spectrum of the inerter displacement is distributed in angular frequencies more broadly. These indicate the mechanical energy in float is transferred to the inerter. The IPA passive control outperforms the CPA passive control by 20.13% in terms of the absorbed energy.

Fig. 18 shows the results comparison between the two systems, under the wave excitation force with $\omega_p = 0.683$ rad/s. Both the passive IPA and CPA have been optimized for $\omega_p = 0.683$ rad/s. In this case, the float response of the IPA is much larger than that of the CPA because the wave excitation frequency is closer to the first modal frequency of the IPA system causing first-mode resonance, while the float of the CPA is not significantly excited because ω_p is far away from ω_f . This further increases the potential of absorbing more energy for the IPA, with an increase of 121.04% in the absorbed energy. The same phenomena that the inerter has a larger response in comparison to the float responses is also observed. Furthermore, the distribution of Fourier amplitude spectra for the IPA float and inerter displacement become narrow and centralized in the first modal frequency in comparison to the CPA float, due to the first-mode resonance.

7. Conclusions

In this paper, an inerter-based point absorber (IPA) WEC with an additional inerter-spring system is proposed for enhanced performance in wave energy absorption, which is also a first step towards establishing an integrated offshore wind and wave energy system. The proposed system can be realized physically by installing tuning springs between the float and the generator, and attaching rotational inertia (a flywheel) to the pulley of generator. The IPA WEC is connected to a fixed structure in the present study, and IPA WEC connected to a floating structure will be investigated in the future.

Under regular waves, analytical solutions of the IPA parameters for maximizing the absorbed energy have been derived, and the optimal parameters all turn out to be dependent on the wave frequency. When the proposed IPA is under active optimal control (parameters vary with wave frequency according to the analytical expressions), its optimal energy absorption, represented by capture width ratio (CWR), is shown to be perfectly identical to the theoretically optimal solution for a

Fig. 16. Wave excitation force. $\gamma = 1.0$. $H_s = 2 \text{ m}$.Fig. 17. IPA passive control in comparison to CPA passive control. $\gamma = 1.0$. $H_s = 2 \text{ m}$. $\omega_p = 0.873 \text{ rad/s}$.Fig. 18. Inerter based passive control in comparison to conventional passive control. $\gamma = 1.0$. $H_s = 2 \text{ m}$. $\omega_p = 0.683 \text{ rad/s}$.

point absorber. This on one hand verifies the correctness of the derived analytical solutions, and on the other hand indicates the outstanding performance of the IPA.

On the basis of the derived analytical solutions, hybrid control and passive control strategies for the IPA WEC have also been proposed and investigated. Comparing with the conventional point absorber (CPA) under the same control strategy (hybrid or passive), the IPA demonstrates consistently superior performance in extracting more power and broadening the operational bandwidth. For the IPA system, it is observed that the response amplitude of the inerter is much larger than that of the float, indicating that the mechanical energy is transferred from the float to the inerter whose motion is directly related to power absorption. This is especially beneficial when the wave excitation frequency is far away from the natural frequency of the float solely (ω_f), as the inerter can still be excited to some extent so that the operational bandwidth is broadened.

Finally, the performance of the passive IPA system is investigated under irregular waves through time-domain simulations and compared with that of the CPA system. This is considered as the most realistic and practical scenario. Parametric optimization of the IPA system with constraints on modal frequencies is employed. The first-mode or second-mode resonance of the proposed system can be achieved when the wave peak frequency is away from the natural frequency of the float (ω_f), while the two modes of the proposed system contribute to the system resonance for wave peak frequencies close to ω_f . This means the inclusion of the inerter-spring system of the IPA facilitates the frequency adaptation of the proposed system, making the system resonate in a broader operational bandwidth. This further leads to a larger efficacy of the IPA system to extract wave energy in comparison to the CPA system. Furthermore, different configurations of the passive IPA can be adapted to tackle the variation of wave peak frequencies of the irregular wave.

Declaration of competing interest

The authors declare that they have no known competing financial interests or personal relationships that could have appeared to influence the work reported in this paper.

Acknowledgments

The support of Aarhus University Research Foundation, Denmark under the AUFF Assistant Professor Starting Grant (AUFF-E-2017-7-20) is highly appreciated.

References

- Al Shami, E., Wang, X., Ji, X., 2019a. A study of the effects of increasing the degrees of freedom of a point-absorber wave energy converter on its harvesting performance. *Mech. Syst. Signal Process.* 133, 106281.
- Al Shami, E., Wang, X., Zhang, R., Zuo, L., 2019b. A parameter study and optimization of two body wave energy converters. *Renew. Energy* 131, 1–13.
- Antonio, F.d.O., 2010. Wave energy utilization: A review of the technologies. *Renew. Sustain. Energy Rev.* 14 (3), 899–918.
- Babarit, A., Clément, A.H., 2006. Optimal latching control of a wave energy device in regular and irregular waves. *Appl. Ocean Res.* 28 (2), 77–91.
- Babarit, A., Delhommeau, G., 2015. Theoretical and numerical aspects of the open source BEM solver NEMOH. In: 11th European Wave and Tidal Energy Conference (EWTEC2015). pp. 1–12.
- Bacelli, G., Nevarez, V., Coe, R.G., Wilson, D.G., 2019. Feedback resonating control for a wave energy converter. *IEEE Trans. Ind. Appl.* 56 (2), 1862–1868.
- Beatty, S.J., Bocking, B., Bubbar, K., Buckham, B.J., Wild, P., 2019a. Experimental and numerical comparisons of self-reacting point absorber wave energy converters in irregular waves. *Ocean Eng.* 173, 716–731.
- Beatty, S.J., Bocking, B., Bubbar, K., Buckham, B.J., Wild, P., 2019b. Experimental and numerical comparisons of self-reacting point absorber wave energy converters in irregular waves. *Ocean Eng.* 173, 716–731.
- Beatty, S.J., Hall, M., Buckham, B.J., Wild, P., Bocking, B., 2015. Experimental and numerical comparisons of self-reacting point absorber wave energy converters in regular waves. *Ocean Eng.* 104, 370–386.
- Budal, K., Falnes, J., 1977. Optimum operation of improved wave-power converter. *Mar. Sci. Commun.* 3 (2), (United States).
- Budal, K., Falnes, J., 1978. Wave power conversion by point absorbers. *Nor. Marit. Res.* 6 (4), 2–11.
- Budal, K., Falnes, J., 1980. Interacting point absorbers with controlled motion. In: Count, B. (Ed.), *Power from Sea Waves*. Academic Press, London, pp. 381–399.
- Clement, A., Maisondieu, C., 1993. Comparison of time domain control law for a piston wave absorber. In: 1993 European Wave Energy Symposium. 21–24 July 1993, Scotland, UK. pp. 117–122.
- Cong, P., Teng, B., Bai, W., Ning, D., Liu, Y., 2021. Wave power absorption by an oscillating water column (OWC) device of annular cross-section in a combined wind-wave energy system. *Appl. Ocean Res.* 107, 102499.
- De Domenico, D., Ricciardi, G., 2018. Improving the dynamic performance of base-isolated structures via tuned mass damper and inerter devices: A comparative study. *Struct. Control Health Monit.* 25 (10), e2234.
- Falnes, J., Kurniawan, A., 2020. *Ocean Waves and Oscillating Systems: Linear Interactions Including Wave-Energy Extraction*, Vol. 8. Cambridge University Press.
- Gao, Z., Moan, T., Wan, L., Michailides, C., 2016. Comparative numerical and experimental study of two combined wind and wave energy concepts. *J. Ocean Eng. Sci.* 1 (1), 36–51.
- Gonzalez-Buelga, A., Lazar, I.F., Jiang, J.Z., Neild, S.A., Inman, D.J., 2017. Assessing the effect of nonlinearities on the performance of a tuned inerter damper. *Struct. Control Health Monit.* 24 (3), e1879.
- Haji, M.N., Kluger, J.M., Sapsis, T.P., Slocum, A.H., 2018. A symbiotic approach to the design of offshore wind turbines with other energy harvesting systems. *Ocean Eng.* 169, 673–681.
- Haraguchi, R., Asai, T., 2020. Enhanced power absorption of a point absorber wave energy converter using a tuned inertial mass. *Energy* 202, 117740.
- Hasselmann, K.F., Barnett, T.P., Bouws, E., Carlson, H., Cartwright, D.E., Eake, K., Euring, J., Gicnapp, A., Hasselmann, D., Kruseman, P., et al., 1973. Measurements of wind-wave growth and swell decay during the Joint North Sea Wave Project (JONSWAP). *Ergänzungsheft Dtsch. Hydrograph. Z. Reihe A*.
- Krenk, S., 2005. Frequency analysis of the tuned mass damper. *J. Appl. Mech.* 72 (6), 936–942.
- Lee, C.-H., Newman, J.N., 2006. *Wamit User Manual*. WAMIT, Inc, p. 42.
- Liang, C., Zuo, L., 2017. On the dynamics and design of a two-body wave energy converter. *Renew. Energy* 101, 265–274.
- Ma, R., Bi, K., Hao, H., 2020. Using inerter-based control device to mitigate heave and pitch motions of semi-submersible platform in the shallow sea. *Eng. Struct.* 207, 110248.
- McCormick, M.E., 2013. *Ocean Wave Energy Conversion*. Courier Corporation.
- Muliawan, M.J., Karimirad, M., Moan, T., 2013. Dynamic response and power performance of a combined Spar-type floating wind turbine and coaxial floating wave energy converter. *Renew. Energy* 50, 47–57.
- Newman, J.N., 2018. *Marine Hydrodynamics*. The MIT press.
- Nielsen, S.R., Zhou, Q., Kramer, M.M., Basu, B., Zhang, Z., 2013. Optimal control of nonlinear wave energy point converters. *Ocean Eng.* 72, 176–187.
- Papageorgiou, C., Smith, M.C., 2005. Laboratory experimental testing of inerters. In: *Proceedings of the 44th IEEE Conference on Decision and Control*. IEEE, pp. 3351–3356.
- Pérez-Collazo, C., Greaves, D., Iglesias, G., 2015. A review of combined wave and offshore wind energy. *Renew. Sustain. Energy Rev.* 42, 141–153.
- Piscopo, V., Benassai, G., Cozzolino, L., Della Morte, R., Scamardella, A., 2016. A new optimization procedure of heaving point absorber hydrodynamic performances. *Ocean Eng.* 116, 242–259.
- Piscopo, V., Scamardella, A., 2021. Parametric design of a resonant point absorber with a fully submerged toroidal shape. *Ocean Eng.* 222, 108578.
- Ren, N., Ma, Z., Fan, T., Zhai, G., Ou, J., 2018. Experimental and numerical study of hydrodynamic responses of a new combined monopile wind turbine and a heave-type wave energy converter under typical operational conditions. *Ocean Eng.* 159, 1–8.
- Ren, N., Ma, Z., Shan, B., Ning, D., Ou, J., 2020. Experimental and numerical study of dynamic responses of a new combined TLP type floating wind turbine and a wave energy converter under operational conditions. *Renew. Energy* 151, 966–974.
- Sheng, W., Alcorn, R., Lewis, A., 2015a. On improving wave energy conversion, part I: Optimal and control technologies. *Renew. Energy* 75, 922–934.
- Sheng, W., Alcorn, R., Lewis, A., 2015b. On improving wave energy conversion, part II: Development of latching control technologies. *Renew. Energy* 75, 935–944.
- Si, Y., Chen, Z., Zeng, W., Sun, J., Zhang, D., Ma, X., Qian, P., 2021. The influence of power-take-off control on the dynamic response and power output of combined semi-submersible floating wind turbine and point-absorber wave energy converters. *Ocean Eng.* 227, 108835.
- Smith, M.C., 2002. Synthesis of mechanical networks: the inerter. *IEEE Trans. Automat. Control* 47 (10), 1648–1662.
- Sugiura, K., Sawada, R., Nemoto, Y., Haraguchi, R., Asai, T., 2020. Wave flume testing of an oscillating-body wave energy converter with a tuned inerter. *Appl. Ocean Res.* 98, 102127.
- Sun, T., Nielsen, S.R., 2018. Stochastic optimal control of a heave point wave energy converter based on a modified LQG approach. *Ocean Eng.* 154, 357–366.

- Wan, L., Ren, N., Zhang, P., 2020. Numerical investigation on the dynamic responses of three integrated concepts of offshore wind and wave energy converter. *Ocean Eng.* 217, 107896.
- Wang, F.-C., Hong, M.-F., Lin, T.-C., 2011. Designing and testing a hydraulic inerter. *Proc. Inst. Mech. Eng. C* 225 (1), 66–72.
- Wang, F.-C., Liao, M.-K., Liao, B.-H., Su, W.-J., Chan, H.-A., 2009. The performance improvements of train suspension systems with mechanical networks employing inerters. *Veh. Syst. Dyn.* 47 (7), 805–830.
- Wu, B., Wang, X., Diao, X., Peng, W., Zhang, Y., 2014. Response and conversion efficiency of two degrees of freedom wave energy device. *Ocean Eng.* 76, 10–20.
- Zhang, Z., 2020. Optimal tuning of the tuned mass damper (TMD) for rotating wind turbine blades. *Eng. Struct.* 207, 110209.
- Zhang, Z., Høeg, C., 2021. Inerter-enhanced tuned mass damper for vibration damping of floating offshore wind turbines. *Ocean Eng.* 223, 108663.
- Zhang, Z., Larsen, T.G., 2021. Optimal calibration of the rotational inertia double tuned mass damper (RIDTMD) for rotating wind turbine blades. *J. Sound Vib.* 493, 115827.
- Zhao, C., Thies, P.R., Ye, Q., Lars, J., 2021. System integration and coupled effects of an OWT/WEC device. *Ocean Eng.* 220, 108405.
- Zhou, Y., Ning, D., Shi, W., Johanning, L., Liang, D., 2020. Hydrodynamic investigation on an OWC wave energy converter integrated into an offshore wind turbine monopile. *Coast. Eng.* 162, 103731.